HHS Public Access

Author manuscript

Cell Rep. Author manuscript; available in PMC 2023 October 23.

Published in final edited form as:

Cell Rep. 2023 September 26; 42(9): 113133. doi:10.1016/j.celrep.2023.113133.

Top-down input modulates visual context processing through an interneuron-specific circuit

Georgia Bastos[1,2], **Jacob T. Holmes**[1], **Jordan M. Ross**[1,3], **Anna M. Rader**[1,2], **Connor G. Gallimore**[1], **Joseph A. Wargo**[1], **Darcy S. Peterka**[4], **Jordan P. Hamm**[1,2,3,5,*]

[1]Neuroscience Institute, Georgia State University, Petit Science Center, 100 Piedmont Ave, Atlanta, GA 30303, USA

[2]Center for Neuroinflammation and Cardiometabolic Diseases, Georgia State University, Petit Science Center, 100 Piedmont Ave, Atlanta, GA 30303, USA

[3]Center for Behavioral Neuroscience, Georgia State University, Petit Science Center, 100 Piedmont Ave, Atlanta, GA 30303, USA

[4]Mortimer B. Zuckerman Mind Brain Behavior Institute, Columbia University, New York, NY 10027, USA

[5]Lead contact

SUMMARY

Visual stimuli that deviate from the current context elicit augmented responses in the primary visual cortex (V1). These heightened responses, known as "deviance detection," require local inhibition in the V1 and top-down input from the anterior cingulate area (ACa). Here, we investigated the mechanisms by which the ACa and V1 interact to support deviance detection. Local field potential recordings in mice during an oddball paradigm showed that ACa-V1 synchrony peaks in the theta/alpha band (≈10 Hz). Two-photon imaging in the V1 revealed that mainly pyramidal neurons exhibited deviance detection, while contextually redundant stimuli increased vasoactive intestinal peptide (VIP)-positive interneuron (VIP) activity and decreased somatostatin-positive interneuron (SST) activity. Optogenetic drive of ACa-V1 inputs at 10 Hz activated V1-VIPs but inhibited V1-SSTs, mirroring the dynamics present during the oddball paradigm. Chemogenetic inhibition of V1-VIPs disrupted Aca-V1 synchrony and deviance detection in the V1. These results outline temporal and interneuron-specific mechanisms of top-down modulation that support visual context processing.

*Correspondence: jhamm1@gsu.edu.

AUTHOR CONTRIBUTIONS

Conceptualization, J.P.H. and D.S.P.; methodology, J.P.H.; investigation, G.B., J.T.H., J.M.R., A.M.R., and C.G.G.; formal analysis, G.B., J.M.R., J.A.W., and J.P.H.; writing – original draft, G.B. and J.P.H.; writing – review & editing, G.B., J.T.H., J.M.R., A.M.R., C.G.G., J.A.W., D.S.P., and J.P.H.; visualization, G.B., J.P.H., and C.G.G.; supervision, J.P.H.; funding acquisition, J.P.H., J.M.R., and D.S.P.

SUPPLEMENTAL INFORMATION

Supplemental information can be found online at https://doi.org/10.1016/j.celrep.2023.113133.

DECLARATION OF INTERESTS

The authors declare no competing interests.

Graphical Abstract

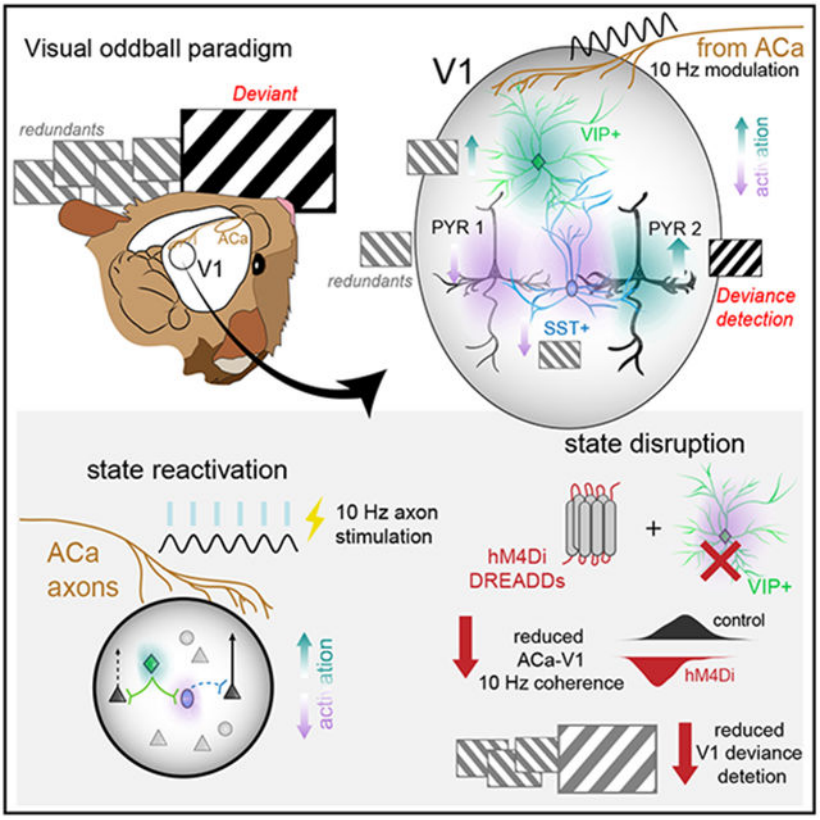

In brief

Bastos et al. studied how the brain processes visual stimuli in context. They find that a prefrontal region, the ACa, modulates the visual cortex, sending spatiotemporal patterns of activity that correlate with stimulus predictability. This engages a VIP-SST interneuronal circuit in the visual cortex to indirectly bolster responses to contextually deviant stimuli.

INTRODUCTION

Sensory data are processed in the neocortex not in isolation but in the context in which they are received. Context can include perceived patterns about the environment–spatial and temporal information–along with any assumed regularities about which stimuli may be typical vs. novel. In the primary sensory cortex, context modulates sensory evoked responses, ultimately influencing attention, learning, and behavior.[1] Understanding how these neuronal circuits incorporate and process contextual information is therefore paramount.

Oddball paradigms are simple and widely used sensory stimulation sequences for studying context processing. An oddball sequence comprises a repeated stimulus (the “redundant”) presented rapidly (≈1.1 Hz) and a rare “deviant” stimulus (the “oddball”) interspersed randomly among the redundant stimuli. In primary visual cortex (V1), evoked neuronal

responses to the redundant stimulus are attenuated, while responses to the deviant stimulus are augmented.[2-4] This augmented activity, termed “deviance detection” (DD), may represent a basic form of cortical “prediction error,” indexing a deviation of current sensory data from the predicted input.[5]

Our recent studies show that only a subset of pyramidal neurons (PYRs) in the V1 exhibit DD and that these neurons are enriched in layer 2/3 (L2/3) of the cortex,[4,6] consistent with theoretical models[7] and empirical reports of visuomotor prediction errors.[8] These DD signals were not present in early evoked potentials or firing responses in L4 of the V1,[2,4,6] suggesting that DD is not inherited from bottom-up/feedforward inputs. On the other hand, DD in the V1 depend on top-down input from a downstream cortical region, the anterior cingulate area (ACa), but axon terminals of ACa neurons in the V1 themselves did not exhibit DD.[4] Together, this suggests that DD responses present in L2/3 of the V1 are not simply inherited from top-down ACa drive but, rather, that they arise indirectly from ACa modulation of V1 circuitry.

In neocortical circuits, heterogeneous classes of cortical inhibitory interneurons play a crucial regulatory role;[9,10] e.g., dictating the gain of PYR responses to modulate feature selectivity to sensory stimuli.[11-15] Although their role during a visual oddball paradigm remains unclear, one possibility is that distinct interneurons types interact to regulate local gain in V1 in accord with context,[16] decreasing excitability among ensembles coding for predictable stimuli (redundants) and indirectly increasing excitability among ensembles coding for non-predicted stimuli (i.e., deviants). Consistent with this idea, we have shown that local somatostatin-positive interneurons (SSTs) in the V1 of mice are necessary for generation of DD,[2] but exactly how SSTs enable DD is unknown. The role of SSTs in DD is particularly unclear, given that SSTs heavily inhibit L2/3 PYRs in the V1, where DD is enriched. Another class of interneurons, vasoactive intestinal peptide-expressing interneurons (VIPs) in the V1, could also be critical for generation of prediction errors, considering their well-established mediation of top-down inputs from the ACa[17,18] and their mutually inhibitory interactions with local SSTs.[19,20] In this paper, we sought to elucidate roles of VIPs, SSTs, and ACa modulation in DD. We hypothesized that VIPs could serve as mediators in top-down modulation of V1 during the oddball paradigm and that this could serve to disinhibit subsets of PYRs by inhibiting SSTs, enabling DD via an Aca-to-VIP-to-SST-to-PYR disinhibitory circuit.

Interneurons can also support the generation and maintenance of cortical oscillations[21] to optimize information processing[22-28] and provide periodic temporal windows that gate or route long-range inputs, structuring their influence on ongoing local processing.[29] For example, during active attentional tasks in non-human primates, top-down/feedback connections in the visual system exhibit activity in the alpha or beta domain (9–25 Hz), while bottom-up/feedforward and local connections exhibit oscillatory signatures in the delta/theta (3–8 Hz) and gamma (25–10 Hz) bands.[30,31] Across cortical regions, DD signals appear to occupy mainly delta/theta frequencies (3–8 Hz) in visual,[2,6] auditory,[32] and multimodal oddball paradigms,[33] supporting the hypothesis that DD signals are prediction errors that are “fed forward” in cortical networks. However, the frequency band the top-down modulation from ACa to V1 occupies in the oddball paradigm has

not been established. We hypothesized that this connection would be expected to show maximal synchrony in the alpha/beta bands, in line with the primate literature,[30] Here we tested these frequency- and cell-type-specific hypotheses of context processing in the V1 during the oddball paradigm. We first replicated the finding that V1 exhibits *bona fide* DD-like responses in the lower theta band (3–8 Hz). We then found that interregional synchrony between the ACa and V1 is strongest in the theta/alpha band, peaking around 10 Hz, and exhibits a "top-down" structure, with phase-amplitude modulation flowing from the ACa to the V1. Further, with two-photon imaging, we showed that L2/3 PYRs exhibit DD in the V1, while VIPs, SSTs, and ACa inputs do not. On the other hand, the VIP and SST activity patterns diverge leading up to the deviant stimulus; VIPs show sensitization (increased responses) to redundant stimuli, while SSTs show enhanced adaptation (decreased responses). This pattern was recreated with rhythmic optogenetic activation of the ACa inputs to the V1 at 10 Hz, suggesting that the 10-Hz synchrony we observed in the local field potential (LFP) experiments served to selectively modulate VIPs and SST responses to redundant stimuli. Finally, chemogenetic suppression of VIPs eliminates ACa-V1 synchrony and DD in the LFP. Our results suggest that contextual modulation of the V1 from the ACa is frequency specific and enables DD in PYRs via a VIP-to-SST disinhibitory circuit.

RESULTS

Signatures of DD in the V1 in the low-theta band

We recorded LFPs simultaneously from frontal and visual cortices of mice while the animal observed a classic visual oddball paradigm. Two bipolar electrodes (contacts separated by less than 400 μm) were implanted in the ACa and V1. The ACa was chosen because (1) it is hierarchically downstream of the V1, (2) it sends dense top-down projections to the V1,[34] and (3) suppressing these projections eliminates DD in the V1 during a visual oddball paradigm.[4] Electrode locations were confirmed postmortem[2,4] (Figures S1A and S1B). Visual stimuli consisted of full-field drifting gratings oriented at 8 possible angles, and responses to select angles were analyzed in three different contexts (Figure 1C): when the stimulus was equiprobable ($p = 0.125$), redundant ($p = 0.875$), or deviant ($p = 0.125$). During recordings, the animals were awake and responsive, head fixed on a small treadmill (Figures 1A-1C). While locomotion is known to impact V1 activity,[35] and whisker movements have been shown to evoke brain-wide responses that extend to the V1,[36] mice did not show differences in these movements across the trial types (deviant, redundant, and control), suggesting that small shifts in behavior evoked by the stimuli were unlikely to explain differences in stimulus processing across contexts in the oddball paradigm (Figures S1C-S1J), consistent with past work.[2,4]

Although rodent studies often use an active behavioral task during sensory processing paradigms as a strategy to ensure attention to the stimuli, here we intentionally employed a passive paradigm. Animals are able to detect unexpected stimuli in the absence of reward anticipation or an explicit goal. Studying this function was the aim of our work. Moreover, recent work has shown that processing rewards or punishments activates VIP activity cortex

wide.[37] This could confound our results because we aim to study the role of VIPs in modulating sensory processing purely with respect to temporal context.

In Figure 1D, individual trial (top) and trial-averaged LFP activity (bottom) shows that the ACa does not elicit a strong visually evoked response, while the V1 does, as expected. The V1 exhibited DD (increased activity to deviant stimulus relative to the control) specifically in lower-theta band (3–8 Hz) stimulus-induced power (Figures 1E and 1F; $F^{STIMTYPE}(1,6) = 8.66$, $p < 0.05$) and intertrial phase locking (Figures 1G and 1H; $F^{STIMTYPE}(1,6) = 10.65$, $p < 0.005$). These results are in accord with previous studies on sensory cortical LFP activity the oddball paradigm.[2,4,38]

Top-down modulation of the V1 in the theta/alpha band during the oddball paradigm

We next analyzed the relationship between LFP activity in the V1 and ACa during the oddball paradigm. We first probed phase locking (1-circular variance) between these regions as a marker of their synchrony (Figure 2A). ACa-V1 interregional phase locking was statistically significant ($p < 0.05$) for frequencies between 1 and 22 Hz and peaked at 10 Hz (Figure 2B). ACa-V1 coherence was ongoing throughout the paradigm and significant even after subtracting the rest period synchrony (Figure 2B, inset). Further, this ACa-V1 coherence was strongest in L1 of the V1, consistent with this reflecting top-down inputs from the ACa to the V1 (Figure 2C) and evidence against the notion that this phase locking reflects remnant volume-conducted hippocampal theta.

Interestingly, the magnitude of this coherence did not differ as a function of stimulus context (Figure 2D), bringing into question how this apparent synchrony relates to context processing during the oddball paradigm. One possibility is that this interregional coherence reflects a bidirectional modulation. Thus, while the overall strength of synchrony between the V1 and ACa may not differ across stimulus contexts, the directionality of the synchrony, or which region “drives” the other, may differ between conditions; e.g., when a current stimulus matches (the ACa drives the V1 during redundants) or betrays contextual regularities (the V1 drives the ACa during deviants).

To test this, we first carried out a non-parametric Granger causality analysis[30] across the frequency spectrum (1–120 Hz) to determine how activity in one region predicts activity in the other region. Interestingly, while we found that the ACa significantly “Granger-caused” V1 activity from 1 to 20 Hz, peaking at 10 Hz (Figures S2A and S2B; $F(1,12) = 13.74$, $p < 0.001$), this magnitude of top-down drive also did not differ between stimulus types either ($F(2,12) = 0.54$, $p = 0.6$). One potential reason for this is that our stimuli were presented highly rapidly (500-ms duration, with 500- to 600-ms ISI) and that changes in low frequencies at physiological lag times (≈ 10 ms) may be too slow to detect.

To address this, we next analyzed long-range phase-amplitude coupling (PAC) between regions under the assumption that changes in power at higher frequencies may exhibit more rapid temporal dynamics. We employed a Granger approach, testing how the phase of low-frequency oscillations in one region (3–39 Hz) predicted the power of high-frequency activity (40–120 Hz) in the other region at a physiologically plausible future time point (i.e., 10 ms). Granger coefficients for long-range PAC were quantified as the F values

representing the change in variance accounted for in power values (Y) in the local region by adding lagged phase values from the distal region (X2; estimated 10 ms in the past) to a model including lagged local power values (X1; also estimated 10 ms in the past; i.e., Y = b1X1 vs. Y = b1X1+b2X2). Using data pooled across trials and time points (−100 ms pre-stimulus to 100 ms post-stimulus offset), change in F values (Granger co-efficients) were calculated bidirectionally (ACa phase to V1 power [“top down”] and V1 phase to ACa power [“bottom up”]) and scaled as percentage of top down minus bottom up divided by the average of both (Figure 2E; averaged across mice and trial types). In general, the phase of ACa low-frequency activity around 10 Hz modulated future V1 high-gamma power (>70 Hz) at higher levels than the reverse direction (positive PAC in Figures 2E and 2F). Previous research has demonstrated that high-gamma power in the neocortex reflects synchronous local neuronal activity[39] and correlates with the fMRI blood-oxygen-level-dependent (BOLD) signal.[21,40] Long-range PAC data from the 10-Hz-phase/70- to 120-Hz-power region in Figures 2E and 2F, quantified for control, redundant, and deviant stimulus conditions, show a stimulus type by direction interaction ($F(2,12) = 11.5$, $p < 0.01$). The phase of ACa-theta significantly modulated future V1-gamma during redundant trials (Figure 2G, $t(6) = 2.60$, $p < 0.05$). This effect was enhanced for later redundants in the sequence (Figure 2H, $t(6) = 2.70$, $p < 0.05$ vs. $t(6) = 0.83$, $p = 0.43$), suggesting that it scales with how well the current stimulus matches predictions and/or perceived contextual regularities that are built on accumulated evidence from preceding trials.[5] There was no clear directionality of information flow under the control condition, and the direction appeared to reverse to deviant (although only at a trend level), suggesting increased bottom-up processing when stimuli betrayed contextual regularities. Other frequencies showing top-down PAC (other regions in the heatmap in Figure 2E), including low and high beta (15–20 and 25–30 Hz) did not show significant stimulus type by direction interactions (Figures S2C and S2D).

To summarize, LFP activity in the ACa in the theta/alpha band appears to lead and predict LFP activity in the V1. This effect was strongest during the redundant stimuli in the oddball run, when bottom-up inputs arising from the stimulus in the V1 are most consistent with the contextual regularities. This suggests that ACa inputs convey contextual information to the V1 about likely current stimuli.

Heterogeneous population dynamics in ACa-V1 circuits during the oddball paradigm

We next investigated the activity of ACa projections to V1 and L2/3 V1 neuron types (VIPs, SSTs, and PYRs) during the oddball paradigm. Our past work showed that, while L2/3 PYRs in the V1 show DD and stimulus-specific adaptation (SSA; i.e., reduced responses to redundant stimuli relative to controls), Aca axon terminals in L1 of the V1 show neither DD nor SSA despite being necessary for DD responses in V1 PYRs.[4] Thus, it is unclear whether and how ACa inputs to the V1 are modulating PYRs. Furthermore, our past work also shows that SSTs too are necessary for V1 DD,[2] but SST activity has not been recorded during a visual oddball paradigm. Thus, it also remains unclear exactly how SSTs support DD.

We carried out fast two-photon microscopy (28 Hz) to record neuronal activity from L1–L2/3 in the V1 as awake mice viewed the oddball and many-standards control sequences

(described above). We imaged the activity of L2/3 PYRs (n = 4 mice, 323 neurons), SSTs (n = 8 mice, 328 neurons), VIPs (n = 9 mice, 284 neurons), and ACa axons in the V1 (n = 4 mice, 100 functionally uncorrelated synaptic boutons and axonal segments). Transgenic mice expressing cre-dependent GCaMP6s crossed with tm1.1-VGluT-, SST-, and VIP-cre-lines were used for soma imaging (Figures 3A-3C), while AAV1-Syn/Cag-GCaMP6s was virally expressed in the ACa to image boutons/axon segments (Figure 3D) in L1 of the V1 as described previously.[4] Only "visually responsive" cells were considered for analysis (89% of neurons recorded for PYRs, 98% for SSTs, 93% for VIPs, and 89% for ACa axons).→

As reported previously,[4] PYRs showed DD (deviant vs. control; $t(320) = 3.17$, $p < 0.005$) and SSA (redundant vs. control; $t(320) = -3.5$, $p < 0.001$; Figures 3A, 3E, and 3F), although DD was present in just 11.5% of PYRs, consistent with our past estimate.[4] This heterogeneity of DD responses across PYRs was not simply explained by differences in stimulus feature selectivity because orientation-selective PYRs (O.S.I. > 0.20) showed DD to their preferred ($t(31) = 2.63$, $p < 0.01$) and non-preferred orientations (Figure 4A; $t(88) = 1.82$, $p < 0.05$). Moreover, non-selective PYRs also showed DD ($t(198) = 1.81$, $p < 0.05$; Figures 4A and 4E), but the magnitude of DD was positively related to the cell's orientation selectivity to the presented stimulus (Figures 4A and 4E), suggesting that DD may reflect a non-specific gain modulation in the V1.

SSTs did not show DD (Figures 3B, 3E, and 3F; $t(326) = 0.53$, $p = 0.60$) but instead showed strong SSA ($t(326) = -6.95$, $p < 0.001$). This suggests that the previously demonstrated role for SST cells in DD[2] is not one of active disinhibition of PYRs during the deviant stimulus but one of indirect disinhibition of PYRs during the buildup to the deviant stimulus through strong SSA. Like DD in PYRs, SSA was present in selective and non-selective SSTs (Figure 4B; $t^{preferred}(20) = -3.91$, $p < 0.001$; $t^{non\text{-}preferred}(35) = -3.72$, $p < 0.001$; $t^{non\text{-}selective}(297) = -5.21$, $p < 0.001$) but scaled with the magnitude of the cell's orientation selectivity index (Figure 4F; $r = 0.291$, $p < 0.001$).

VIPs also did not show DD (Figure 3C; $t(282) = 1.2$, $p = 0.233$) but, surprisingly, showed inverse SSA; that is, VIPs were, on average, more active to redundant stimuli ($t(282) = 2.82$, $p < 0.005$). Given known mutual inhibition between VIPs and SSTs, this augmentation of VIP activity to the redundant may give rise to the enhanced SST adaptation to redundant stimuli. Interestingly, only selective VIPs showed statistically significant inverse SSA, and they only displayed it to their preferred orientation (Figures 4C and 4G; $t^{preferrred}(15) = 2.19$, $p < 0.05$), suggesting heterogeneity in this cell population.

In our past work, we showed that ACa inputs to the V1 were necessary for DD.[4] In a subset of mice (n = 4), we replicated this effect here via optogenetic suppression of ACa inputs (Figure S3; $F^{interaction}(1,140) = 4.69$, $p < 0.05$). Despite this clear role, stimulus-responsive ACa axons in our current study did not vary as function of context (Figures 3D-3F; redundant vs. control: $t(87) = -0.17$, $p = 0.87$; deviant vs. control: $t(87) = -0.56$, $p = 0.58$; Figure 4D). A closer analysis of ACa axon activity, however, evinced greater variance across the population of inputs during the oddball paradigm compared with the many-standards control (Figures 4H and 4I; Bartlett's test statistic$^{ctrl_vs_rdnt} = 4.60$, $p < 0.05$; $BTS^{ctrl\_vs\_dev} = 11.6$, $p < 0.001$; $BTS^{dev\_vs\_rdnt} = 1.70$, $p = 0.20$). This suggests a wider

spread of input magnitudes, including more highly active and more mostly silent inputs during the oddball, when the context is more defined (i.e., when one orientation is highly likely). On the other hand, during the control paradigm, when the context is more general (8 possible orientations), there was a more Gaussian spread of ACa-V1 input magnitudes across the population of axons. Further, we found that the stimulus orientation (135° vs. 45°) could be decoded from the early (0–84 ms; first 3 frames) activity in ACa axons only during the oddball paradigm (when the orientation of the upcoming stimulus was predictable) but not during the control sequence (when the upcoming stimulus was not predictable; Figures S4A-S4C; $\chi^{2\text{–control}}(6) = 7.92$, $p = 0.25$; $\chi^{2\text{-redundant}}(6) = 13.4$, $p < 0.05$; $\chi^{2\text{-deviant}}(6) = 12.8$, $p < 0.05$; leave-one-out cross-validation: control, 50% [chance]; redundant, 70%; deviant, 70%). Conversely, stimulus orientation could be decoded from V1-PYR data for all trial types, as expected, because the V1 is responding to the current stimulus, not the contextually most likely stimulus (Figures S4D and S4E).

Altogether, like in the LFP data, this suggests that ACa input to the V1 conveys contextual information about the likely upcoming stimulus, which modulates V1 in such a way that incoming sensory data that betray contextual regularities are readily “detected” and elicit DD responses. How is this achieved? One possibility is that top-down input from the ACa serves to amplify feature-selective VIP responses. This amplification of VIP activity would cause them to “win out” against SSTs in highly predictable contexts, effectively disinhibiting subsets of PYRs during the redundant phase of the paradigm. This disinhibition, stemming from reduced SST inputs, would then prime certain PYRs for DD responses to a contextually deviant stimulus.

Top-down drive of the V1 from the ACa in the theta/alpha band activates VIPs and suppresses SSTs

To test this hypothesized ACa modulation of VIP-SST circuits in the V1, we first optogenetically activated ACa inputs to the V1 during rest. Based on our above results (Figures 2-4), we predicted that driving these axons at theta/alpha frequencies (6–10 Hz; peak ACa-V1 synchrony band) should increase activity of V1 VIPs and PYRs while decreasing activity of SSTs. Rhythmic wide-field optogenetic stimulation of axons from ACa excitatory cells was performed with channelrhodopsin (ChR2) through a craniotomy over the V1 (Figure 5A). Activity of PYRs, VIPs, or SSTs was imaged in the V1 while ACa axons were activated at 2, 6, 10, 20, or 40 Hz, a power-normalized “weak” block stimulation, and a full-power block stimulation (Figures 5A, 5B, and S5).

The effects of ACa drive on the V1 differed depending on cell type and frequency (Figure 5C; $F(10,4,035) = 9.60$, $p < 0.001$). During 6- and 10-Hz stimulation, PYR and VIP responses differed from SST interneurons, with VIPs and PYRs increasing their activation while SSTs decreased below baseline (all $p < 0.001$). An LED-only control condition ruled out the possibility that these effects were caused by either heat or light-only artifactual responses (Figures S6A and S6B). Consistent with our hypothesis, cell-specific responses to top-down theta/alpha activation point to a possible VIP-to-SST-to-PYR disynaptic disinhibitory motif, although some activation of PYRs during our optogenetic stimulation could result from direct synapses of ACa on PYRs.[17]

It was also apparent that 40-Hz stimulation strongly activated VIPs. Past work on ACa-V1 circuitry showed that top-down gamma-band drive of ACa projections to the V1 promotes post-error performance during an active visual attention task.[18] Because we did not observe strong ACa-V1 gamma synchrony during our task-free paradigm, it is possible that top-down theta/alpha and gamma activation of the V1 engages different circuit motifs. Consistent with this notion, heterogeneity within SST, VIP, and PYR groups to top-down drive was apparent (Figure S6A). To determine whether there were specific ensembles of cells, reaching across cell classes, that activate to different frequencies of top-down drive, we carried out a k-means clustering analysis on the standardized opto-evoked responses, collapsing across VIPs, SSTs, and PYRs (STAR Methods). Results from a shuffling procedure and a visual inspection of a scree-plot together suggest the presence of 6 stimulation clusters (Figure 5D). One cluster represented non-stimulated cells (about half of cells recorded), and two minor stimulation clusters represented less than 2% of imaged cells (likely outliers). The remaining three major stimulation clusters all comprised greater than 12% of imaged neurons each. Clusters 1 and 2, which showed strong responses to gamma stimulation and theta/alpha stimulation (Figure 5F), respectively, contained primarily VIPs and PYRs with very few SSTs (Figure 5G). Clusters 1 and 2 showed significant responses to 10-Hz stimulation relative to the non-rhythmic block stimulation (paired-samples t tests, $p < 0.01$). On the other hand, cluster 3 was a broad suppression cluster that included mostly SSTs. However, there was no specific effect at 10-Hz or any frequency-relative block stimulation. Thus, top-down drive inhibits SSTs regardless of frequency, but it activates VIPs best at either 10 Hz or 40 Hz.

VIP interneurons mediate ACa modulation of the V1 and support DD

These results suggest that VIPs mediate ACa-to-V1 modulation, which is active at ≈ 10 Hz (Figure 2) and critical for DD in the V1 (Figure S3).[4] To more directly test this, we used a chemogenetic strategy (hM4Di) to selectively suppress VIPs in the V1 while recording LFPs during the oddball paradigm.

In the experimental group, but not the CNO-only control, VIP suppression via CNO led to an increase in baseline power (inter-stimulus intervals) in the V1 (Figure 6B, left; $F^{interaction}(1,11) = 5.08$, $p < 0.05$), confirming a basic disinhibition of the V1 by removing a source of inhibition. Consistent with our hypothesis that VIPs mediate ACa-V1 modulation, interregional synchrony between the ACa and V1 in the ≈ 10-Hz range decreased after VIP suppression (Figure 6C, left; $F^{interaction}(1,11) = 5.02$, $p < 0.05$). Further, VIP suppression also eliminated DD in the aggregate LFP in the V1, specifically in stimulus-induced power in the low theta-band (3–8 Hz; Figures 6C-6F and S7; $F^{interaction}(1,11) = 12.67$, $p < 0.01$).

DISCUSSION

The current results suggest a detailed spatiotemporal mechanism for the ACa's role in visual DD (Figure 7). During a simple visual oddball paradigm, ACa modulates V1 activity in theta/alpha frequencies, engaging a mutually inhibitory VIP-SST circuit in the V1 that effectively disinhibits subsets of V1 PYRs. These disinhibited subsets of PYRs are then potentiated to respond strongly to future non-predicted stimuli (e.g., DD). This model

(Figure 7) is supported by evidence showing that (1) the Aca and V1 synchronize at 10 Hz during the oddball paradigm; (2) this synchrony shows strong Aca-to-V1 directionality during contextually redundant stimuli; (3) SSTs show strong response suppression during redundant stimuli and 10 Hz stimulation of ACa inputs, while (4) VIPs show response facilitation during redundant stimuli and 10-Hz stimulation of ACa inputs; and (5) that suppressing VIPs disrupts ACa-V1 synchrony and V1 DD.

Oddball processing in a predictive coding framework: Top-down predictions and bottom-up prediction errors

One popular generalized framework for understanding context processing in the mammalian neocortex is "predictive processing."[5,41,42] Here, the inferred causes of sensory inputs—or predictive models of the environment—are encoded in hierarchical cortical networks.[5,43] Stimuli that deviate from this model elicit "prediction errors" in lower sensory cortices (putatively, DD), which then propagate to higher areas to update the predictive model of the environment (i.e., of the underlying causes of sensory input).[7,44,45] Evidence in support of this predictive model of sensory processing in the cortex spans sensory modalities in multiple mammalian species, from humans[46,47] to rodents.[8,30,33]

Our results provide some evidence that oddball processing can be understood in this framework because top-down modulation of primary sensory regions is necessary for DD (putatively, prediction errors) and appears to signal the likely upcoming stimulus (putatively, predictions; Figures S4A-S4C). Although our work here and elsewhere suggests that DD responses during the oddball paradigm fit many of the predictions of the predictive processing framework, including a strong presence in feedforward layers of the cortex,[4,6] a strong theta and gamma band signal,[6] increased bottom-up directional flow in cortical networks (Figure 2G), and hierarchical expression across distributed cortical networks,[33] whether such DD responses truly serve to "update" internal predictions is not strictly discernable from the current data. Thus, interpreting the current results as evidence of predictive processing is not yet fully warranted, and other theories may also hold weight. For instance, the fatigue model suggests a passive mechanism explaining DD: as one neuronal population becomes adapted, it leaves others "fresh" and more responsive to incoming novel stimuli.[48] Notably, our manipulations show that adaptation (SSA) appears to be mechanistically separate from DD in L2/3 (Figure S3). How the inverse adaptation among some VIPs (Figure 3) fits into this fatigue model is also unclear.

Top-down modulation influences local cell activity through a distinct frequency channel

Connectivity clearly influences cortical information processing, but the temporal dynamics within these connections may serve to further segregate or route interregional signals to activate or suppress specific ensembles.[30,49] Our results show that, during a predictable sequence of visual stimuli, the ACa and V1 synchronize in the theta/alpha band. Our optogenetic driving experiments show that top-down input in a distinct frequency band may potentiate VIPs and suppress SSTs. This same pattern of increased VIP activity and decreased SST activity was observed during the redundant phase of the oddball paradigm, when top-down theta/alpha influence was strongest. This suggests that top-down modulation

in this specific frequency range may engage the VIP-SST mutually antagonistic circuit necessary for passive visuospatial[10] and temporal[2] context processing in the V1.

Past work in this circuit has shown that the ACa may naturally send high beta-band signals during a behavioral error[18] and that ACa-to-V1 projections target PYRs as well as multiple interneuron types (PVs, SSTs, VIPs, etc.) to mediate disynaptic inhibition and support visual attention.[17] Our study complements this by identifying a lower, theta/alpha-band oscillation during non-goal-directed visual processing and its effect on V1 interneuron types. The precise frequency ranges involved in feedback and feedforward signals, however, may differ between regions and animal models. As mentioned previously, in directed attention tasks with NHPs, feedback activity is driven at the alpha/beta bands, while theta and gamma bands are associated with feedforward signals.[30,31] It is possible, however, that our theta/alpha range (6–12 Hz) could be functionally similar to these studies' alpha/beta range (10–20 Hz). The exact discrepancy could be due to simple differences in brain size between mice and NHPs, the nature of the task itself (active vs. passive paradigms), or the exact brain regions chosen.[30,31] Nevertheless, our results are consistent with the core idea that frequency channels serve as a routing mechanism for feedback modulation and feedforward information.[30]

Interneuron microcircuits support context processing in the V1

In Figure 7, we provided a schematic to help explain our results and, importantly, to guide future experiments. This model is based on current and past observation and rests on some heretofore untested assumptions. For one, it is assumed that there is some connection specificity among feature-selective VIPs, SSTs, and PYRs. While our results do show that modulations to the redundant stimuli are strongest in VIPs and SSTs that are selective for the redundant stimulus (Figures 4F and 4G), the notion that VIPs and SSTs target distinct subnetworks of feature-selective PYRs is a key aspect of our model that is only partially supported in the literature.[50] Future work is necessary to more comprehensively test this $ACa^{long\text{-}range}$-VIP^{V1}-SST^{V1}-PYR^{V1} DD circuit, including studies that selectively inhibit each element while imaging the other, during different phases of the paradigm. Another important (though technically challenging) future experiment would be to selectively inactivate ACa inputs to V1-VIPs only, testing whether long-range coherence and ACa-dependent DD in V1 is truly dependent on the Aca-to-VIP circuitry specifically or whether ACa inputs to PYR apical dendrites also play a role. Further, more work is needed to investigate the roles of other cell types within the V1, including parvalbumin-positive interneurons (PVs) and neurogliaform cells in L1.

A recent study of visual cortical activity reports a similar pattern of adaptation and facilitation in SSTs vs. VIPs, respectively.[51] Our study adds to this work, suggesting that top-down inputs from the ACa that preferentially activate VIPs (Figure 5) may play a role supporting this VIP facilitation and SST adaptation. Still, key differences in our paradigm and that of Heintz et al.[51] exist. For one, Heintz et al.[51] used a continuous 10-s stimulus followed by 10 s of blank screen, while we used a typical oddball paradigm, which has trains of repeated 500-ms stimuli with 500-ms blank screen inter-stimulus intervals, recurring once per second for up to 8–9 s and including presentation of an opposite (deviant) orientation.

Thus, the degree of recovery from train to train is likely not comparable between these two paradigms. Further, the adaptation effects we identify (Figure 3) reflect contextual adaptation—comparing responses with the same stimulus when it is redundant (in the oddball run) vs. not redundant (in the many-standards control run)—while Heintz et al.[51] studied a shorter-term adaptation response to a continuous stimulus (an effect that cannot be ascertained from the current study). Therefore, whether the adaptation pattern that they identify arises from similar mechanisms identified in the current study requires future study.

Our results suggest that VIPs mediate top-down modulation of the V1 to generate differential responses to predictable vs. unexpected stimuli (i.e., DD); i.e., they distribute contextual information from higher cortical areas (Figure 4). This notion is largely consistent with past work in VIPs in the neocortex. The fact that VIPs are concentrated in superficial cortical areas, which receive the majority of top-down inputs from higher regions, positions them to mediate disynaptic inhibition and disinhibition of multiple cell types.[52] Evidence of such motifs has been found in multiple regions of the mouse cortex[19,35,50,52-54] and serves to elicit differential responses in brain networks depending on the task, context, and behavioral state. For example, VIPs play a disinhibitory role in modulating PYR neuron activity by inhibiting other interneuron types, PVs, and SST neurons.[19,53] This may be particularly pronounced during locomotion.[55] In the current study, we did not find that mice exhibited context- or stimulus-driven locomotion, so the modulatory role of VIPs in our paradigm cannot be simply explained by this function.

Much of the past research done on the role of cortical VIPs during visual novelty processing has involved mice in the presence of a trained behavior output, often conditioned through reward and punishment, and locomotion as a part of the behavior.[35,37,55,56] In this study, we sought to understand the functional dynamics of VIP interneurons in a passive oddball paradigm in the absence of an active report or anticipated reward. Notwithstanding the fact that passive, untrained, or non-goal-driven behavior makes up a large part of any animal's natural life, the value of a strictly passive oddball paradigm is clear from the clinical neurophysiology literature. One of the best replicated biomarkers of schizophrenia (SZ), the mismatch negativity (an electroencephalogram [EEG] index of DD), involves a purely passive sensory sequence (i.e., the oddball sequence).[3,38,57] Interestingly, our finding that VIPs are more strongly active to predictable stimuli contrasts some findings where VIPs were shown to have higher activation to novel images in comparison with familiar ones.[56,58] A key difference here may be the nature of the paradigm. Garret et al.[56] used a directed task that involved locomotion and reward: two factors that have been shown to independently lead to VIP activation.[37,56] Therefore, it is unclear whether past findings of VIP activation to novel stimuli are associated with the novel stimulus itself, with the reward administration, past experience linking rewards to visual stimuli, or a combination thereof. Notably, we did find a small subset (≈4%) of VIPs that exhibited DD (Figure 3H).

Top-down input to the V1 is modulatory and necessary for DD

Our past work has shown that top-down inputs from the ACa to the V1 are necessary for visual DD via optogenetic silencing.[4] We replicated these results in the current study (Figure S3). The notion that top-down feedback in cortical circuits is necessary for generating

DD is consistent with the predictive processing framework. That is, top-down inputs are carrying predictions (or contextual information) not evoked by the current stimulus but instead signaling what the internal model holds that the current stimulus could be. When the bottom-up signals (i.e., the inputs from the thalamus/L4) concord with the predictions of the internal model, the activity of V1 is dominated by top-down inputs. Our Granger analyses of LFP data are consistent with this interpretation because the aggregate LFPs in the ACa appear to lead and predict the aggregate LFPs in the V1 during the redundant stimuli; i.e., theoretically, when the bottom-up and top-down match. Exactly which cells are being modulated by ACa inputs selectively and more strongly during the redundant trials remains to be shown explicitly, but our data point toward VIPs. On the other hand, when bottom-up and top-down signals do not match (i.e., during deviant stimulus), responses are enhanced, leading to most of the V1 activity to be driven locally or even in the bottom-up direction (V1 to ACa).

In further support of the interpretation that ACa axons are sending predictive information to the V1, the variance of activity across the ACa population was wider during the oddball compared with the many-standards control (Figures 4H and 4I), This suggests that activity of top-down inputs was more precise, including more active and more non-active ACa boutons, when the probability of the next stimulus was more certain (i.e., during the oddball paradigm, when it was very likely the redundant stimulus) compared with when the next stimulus could be one of 8 orientations (i.e., during the control paradigm). Interestingly, the variance of axonal activations did not differ between the redundant and the deviant stimuli during the oddball paradigm, further suggesting that ACa-V1 inputs do not convey stimulus-evoked activity back to the V1, but, rather, that they comprise anticipatory inputs containing the predictive information.

Our decoding analysis of ACa axonal activity also supports this interpretation, suggesting that early ACa input activity could be used to decode the likely upcoming stimulus only during the oddball paradigm, when the stimulus was predictable (Figures S4A-S4C). Further, the population vectors for the ACa project in nearly opposite directions for the deviant vs. redundant trials of the same stimulus orientation (Figure S4B-S4C), suggesting again that ACa activity is predicting the stimulus, not responding to the stimulus.

One apparent challenge to this interpretation is that silencing of ACa inputs does not seem to affect SSA in PYRS during redundants (Figure S3; [4]). In a simple interpretation of the V1 dynamics in the oddball paradigm, SSA would reflect the “predictive suppression” present in predictive processing (while DD reflects prediction error). If this is true, then why doesn’t optogenetic suppression of the ACa (which theoretically carries the predictions to V1) eliminate SSA? We propose that the V1 activity modulated by ACa inputs during the redundant stimulus train is not related directly to SSA and may be obscured by strong SSA. For one, ACa drive at 10 Hz modulated SSTs and PYRs in opposite directions (Figure 5) despite both populations exhibiting SSA (Figure 3). Second, based on our past work, SSA is likely inherited in the bottom-up inputs to L2/3 (and perhaps in thalamocortical inputs) because it is present in early evoked potentials in L4 and in PYR neurons in all layers[4,6] (unlike DD). Third, SSA was also not affected by suppression of local V1 interneurons like DD.[2] Altogether, these points suggest that DD and SSA rely on distinct mechanisms

rather than being complementary effects of the same predictive process. Based on this, we propose that the oddball paradigm is not optimal for studying top-down predictive suppression because too much bottom-up adaptation is present (in the form of SSA). A paradigm utilizing a predictable visual sequence without stimulus repetition[16,59] may help directly test whether and how top-down inputs to the V1 underlie predictive suppression.

Limitations of the study

The current study utilized a classic but simple paradigm for studying context processing: the oddball paradigm. This choice was deliberate because the oddball paradigm has a long history in studies of SZ (e.g., see "mismatch negativity," a DD analog measured by EEG[38,57,60]). However, to more broadly understand context processing and the cortical circuits responsible, it would be critical to (1) examine other sensory modalities; (2) vary parameters systematically, such as stimulus feature, deviation magnitude, deviant probability, etc.; and (3) include a predictable sequence without stimulus repetition (see above).

Further, we did not identify any behavioral measure that was significantly different during the deviant stimuli (Figure S1), suggesting that small behavioral responses could not account for our differences in visual context processing in the same manner that it can account for, e.g., cross-modal responses in the V1 to auditory stimuli.[36] Still, it remains possible that behavioral state could modulate how deviants are processed. For example, concurrent locomotion may increase the magnitude of DD. Our current study was not designed nor powered to address this issue because the classic oddball paradigm involves rapid (1.1-Hz) stimulus presentations and limited repeats of the same stimulus to avoid longer-term plasticity effects. Future works should explore this notion because it is possible that behavioral state could play a modulatory role in visual adaptations (but see, e.g., Heintz et al.[51]).

While our analysis of ACa axon population patterns may suggest that the cortex sends top-down predictive information during the oddball paradigm (decoding, standard deviation; Figure S4), we urge caution in drawing a strong conclusion from our relatively limited scope of recordings. A wider sampling of stimulus feature space and a broader recording of the V1, with many more axonal inputs and behavioral covariates, is needed to fully test this notion.

Additional experiments remain to test our model more thoroughly (Figure 7). While a number have been mentioned above, a key point is that it relies on some selectivity in VIP-to-SST or VIP-to-PYR targeting with respect to stimulus preference. This remains to be shown. Further, our effects of VIP silencing on DD in the V1 were shown only in the aggregate LFP. While measurements of DD and, more specifically, visual mismatch negativity have classically used aggregate LFP or EEG measures, future work should confirm that this effect is also seen at the single-cell level, particularly in PYRs, after suppressing VIPs. Finally, while we intentionally studied stimulus processing in the absence of a behavioral task or reward contingency, understanding the behavioral effects of DD responses, immediate and longer term, remains key.

STAR★METHODS

RESOURCE AVAILABILITY

Lead contact—Further information and requests for resources and reagents should be directed to and will be fulfilled by the lead contact, Jordan Hamm (jhamm1@gsu.edu).

Materials availability—No new reagents or materials were generated for this study.

Data and code availability

- All data has been deposited at Zenodo and is publicly available as of the date of publication.[61] https://doi.org/10.5281/zenodo.8273225.
- All original code for analyzing the data has been deposited at Zenodo and is publicly available as of the date of publication.[62] https://zenodo.org/record/8335415 and https://doi.org/10.5281/zenodo.8335415
- Any additional information required to reanalyze the data reported in this paper is available from the lead contact upon request.

EXPERIMENTAL MODEL AND STUDY PARTICIPANT DETAILS

Experiments were carried out under the guidance and supervision of the Georgia State University (GSU) Division of Animal Resources and were approved via Institutional Animal Care and Use Committee (IACUC) at GSU. Adult C57BL/6 mice (n = 49, age range from P51 to P167, from Jackson Laboratories) were used. Mice were weaned at P25 and group housed (max 5 mice per cage) separated by sex. They were maintained at a 12/12 light/dark cycle (light: 6a.m.-6p.m.) with food and water available *ad libitum.* Animal ages varied between P51(min) and P167 (max) and averaged at 105 days. Experimental mice were chosen randomly based on availability and age; both female and male mice were included in similar proportions (25F, 24M). Transgenic lines were made using mice expressing cre-dependent GCaMP6s (tm162(tetO-GCaMP6s, CAG-tTA2)) crossed with tm1.1-(VGluT-), SST- and VIP-cre lines.

Surgical procedures—For experiments involving calcium imaging, head-plate fixation and craniotomy surgeries were carried out together as previously described.[4] Briefly, a hole with a 3 mm diameter was drilled in the mouse skull in left V1 (coordinates from bregma: X = 2 mm, Y = −2.92 mm), followed by the removal of the skull and exposure of brain surface; dura matter was conserved. A cover glass was placed and sealed at the hole location. Then a titanium head-plate was attached to the mouse head to allow for head-fixation during imaging. For calcium imaging or optogenetic manipulation of ACa axons, virus injections were done 2 to 3 weeks prior to head-plate fixation and craniotomies. A small hole was drilled in the mouse left ACa (coordinates from bregma: X = 0.35 mm, Y = 1.98 mm, Z = 0.9 μm from brain surface); a micro-syringe attached to a stereotaxic apparatus was used to deliver 0.75 μl of a 1:1 solution of PBS and channelrhodopsin (pAAV9-CaMKIIa-hChR2(H134R)-mCherry), ArchT (pAAV9-CaMKIIa-ArchT-GFP), or GCaMP6s (pAAV.Syn/Cag.GCaMP6s.WPRE.SV40) over a 10 min period (0.075 μL/min) to each mouse.

For local field potential experiments, head-plate attachment was carried out prior to electrode implantation. Two bipolar electrodes twisted together (with contacts spaced approximately 200 μm apart) were inserted below the dura in stereotaxically defined ACa and V1 (coordinates from bregma: ACa, X = 0.35 mm, Y = 1.98 mm; V1, X = 2 mm, Y = −2.92 mm) approximately 0.5mm between the dura and white matter, and grounded on the skull contralateral to the target areas, totaling 4 contacts for each region (two at target, two grounded). For experiments with LFP and VIP chemogenetic suppression, 0.75 μL of 1:1 diluted AAV8-hSyn-DIO-hM4Di-mCherry was injected in left V1 (coordinates above) starting at 0.9 mm deep and moving up to 0.5 mm from the brain surface continuously during the whole injection period (at a rate of 0.04 mm/min) to assure an even and widespread expression of the virus. Injections were done in VIP-cre mice at the same time as head-plate fixation, approximately 3–4 weeks prior to recordings. All animals that went through surgery were anesthetized using 3% isoflurane and received pre and post care medication appropriately (5 mg/kg carprofen, IP). Prior to recordings, mice underwent at least 3 training sessions to acclimate them to head-fixation and the visual stimuli, as previously described.[63]

METHOD DETAILS

Visual stimulation—Visual stimulation was presented on a flat TV screen at a 45° angle from the animal axis, approximately 15 cm from the eye, using Psychophysics Toolbox on MATLAB (Mathworks). Full-field, black and white, sinusoidal moving gratings were presented at 100% contrast, 0.08 cycles per degree, drifting at two cycles per second, at eight possible orientations (30°, 45°, 60°, 90°, 120°, 135°, 150°, and 180°). Stimuli were presented for 500 ms, with an inter-stimulus interval of 500 ms of black screen. A “many-standards control” (equally rare, randomly presented stimuli at all 8 possible orientations) was presented before each oddball sequence to establish baseline activity. The oddball sequence consists of a repetitive sequence of one stimulus (“redundant”, either 30°, 45°, or 60° degree angles, presented 87.5% of the time), randomly interrupted by a stimulus of a different orientation (“deviant”, 120°, 135°, or 180° degree angles, presented 12.5% of the time). In the latter half of the sequence, the redundant stimulus is “flipped” to become the deviant, and vice versa (“oddball flip”); thus, we can assess responses to the stimulus context (i.e., in what context a stimulus is shown) rather than stimulus features (i.e., what orientation a stimulus is).

Optogenetic stimulation with LEDs—One second bursts of 473 nm light delivered through an LED (Bruker optogenetics module) was focused to 100 μm below the surface of V1 to activate ACa axons at 2-, 6-, 10-, 20-, or 40 Hz (20% duty cycle, squarewave pulses; .5 mm radius; 12 mW per mm^2 at the surface), a power-normalized “weak” block stimulation (delivering the same overall power per second as the rhythmic stimulations – 2.4 mW per mm^2), and a full-power block stimulation (1 s of 12 mW per mm^2). These seven conditions were carried out in random order and interspersed with 9 s of rest between them, and each condition was repeated 10 times. No visual stimulus was shown in this run. Black tape was placed around the objective to prevent spillage of the blue light into the animal’s eyes. Virus expression and stable drive of these neurons were confirmed via histology (Figures S5A and S5B) and LFP recordings in ACa during V1 drive (Figures S5E-S5H).

Optogenetic silencing of ACa inputs to V1 was carried out with a similar procedure in 4 mice, but with 617 nm and starting 100ms pre-stimulus onset to 100ms post-stimulus offset, every third trial (Figures S3D, S3H-S3J).

2-Photon calcium imaging—Two-photon microscopy (28 Hz framerate; Bruker Investigator laser scanning microscope; Bruker Corporation, Billerica, MA, USA) excited by a laser (Chameleon Ultra II, Coherent Inc, Santa Clara, CA, USA) at 920nm wavelength were used to image the fluorescent calcium sensor GcAMP6s expressed in PYRS, VIPS, SST cells and ACa axons in the mouse visual cortex. The laser beam was modulated with a Pockels cell (Conoptics 350-105, with 302 RM driver) and scanned with galvometers through a water immersion objective (16X/0.80W, Nikon, Tokyo, JP). The objective lens was positioned over the animals head while a small volume of Aquasonic ultra-sound gel (Parker Laboratories Inc) was placed at the site of the cranial window to bridge the objective with the imaging area and stabilize over long-duration sessions. The animals were awake, head-fixed to the microscope by their headplate, while sitting on top of a wheel free to move forward and backwards. All recordings were carried out in a dark room with the researcher present to monitor mouse wakefulness and check for signs of discomfort. Each run had a duration between 6 and 7 min. Scanning and imaging were done through Prairie View (Prairie Technologies) software (resonant galvo, downsampled to 28 frames per second, for 256 × 256 pixels, 3.136 μm pixel size, 802.9 × 802.9 μm field of view). A time-series was recorded using Prairie View software as the mice observed visual stimuli or received opto-drive. The visual stimulus was transmitted to the monitor through an HDMI cable, converted to a voltage trace, and connected to the computer through the Voltage Recording tool on Prairie View. Time-series and stimulus voltage traces were synchronized at the onset of recording for proper alignment of neuronal activity and stimulus presentation. Optogenetic drive waveforms were converted to voltage traces and recorded through Prairie View in a similar fashion, with the signal transmitted both to the light-stimulation driver and the computer. For PYRS, VIPs and SST recordings, images were taken 100 μm-350 μm from the brain surface, approximately L2/3 of the mouse cortex. For ACa axons, recordings took place at 50–100 μm deep, approximately L1 of mouse cortex.

Local field potentials recordings—For the LFP experiments, the mouse was fixed to the recording apparatus through the head-plate and free to move back and forth. Insulated cables were connected to the implanted electrodes and plugged into a differential amplifier (Warner instruments, DP-304A, high-pass: 0 Hz, low-pass: 500 Hz, gain: 1K, Holliston, MA, USA). Amplified signals were passed through a 60 Hz noise cancellation machine (Digitimer, D400, Mains Noise Eliminator, Letchworth Garden City, UK), which, instead of filtering, creates an adaptive subtraction of repeating signals which avoids phase delays or other forms of waveform distortion. Multielectrode probe LFPs (Figure 2C) were recorded as previously described,[6] from a custom designed 16-channel NeuroNexus probe (750 μm length, 50 μm inter-contact distance; A1 × 16–3 mm 50–177; Ann Arbor, MI) inserted perpendicularly into left V1 at 100 μm/min until the dorsal-most electrode was just below the dura (deduced from real-time signals). Prior to insertion, probes were submerged in DiI dye for post-hoc anatomical validation. These LFP data were acquired from 0.1 to 7500 Hz upper and lower bandwidths, sampled at 10 kHz, and then low-pass filtered at 150 Hz

and resampled at 1 kHz for preprocessing. Electrophysiological activity was recorded using the Prairie View software or with an Intan Recording system (multielectrode recordings). Visual stimulus timings were recorded as voltage traces at the same time as the LFPs signals for proper alignment, and the timing of these stimuli relative to LFP recording was confirmed with photodiodes placed on the video monitor. For VIP suppression, the animals were injected with CNO immediately following the completion of the first recordings (IP, 5 mg/kg)[2] and recorded again after 30 min.

QUANTIFICATION AND STATISTICAL ANALYSIS

2-Photon image processing and analysis—Videos were corrected for motion using the "moco" plugin on ImageJ.[64] Cellular activity was semi-manually scored using custom MATLAB scripts, as previously described.[63] Mean and standard deviation were calculated for all image frames and plotted for reference; ROIs were manually selected around cell bodies/axon segments through a GUI in MATLAB. A PCA analysis was performed within the selected regions of interest (ROIs) to select the pixels with weights at least 80% of the maximum of the first PCA component as the final ROI, then plotted as an average fluorescence across pixels. The fluorescence time-courses were displayed after each selection to verify stability across imaging experiments and healthy calcium transients. Halo subtraction was performed in the selected ROIs to exclude excess fluorescence from nearby cells. For scoring axonal/bouton ROIs, datasets were first downsampled to 9.4 frames per second to aid in scoring and detection. This is consistent with our past analysis[4] and was necessary due to the fact that such small ROIs have faster transients and smaller signal to noise ratios. For analysis, time-courses were re-interpolated to 28 frames per second for comparison with other cell types (PYRs, VIPs, SSTs). Effectively, this was equivalent to a 3-sample Gaussian smooth. For axon segments and boutons, we attempted to exclude ROIs originating from the same cell (i.e., we focused on those which were apparently functionally independent). That is, segment/bouton pairs showing highly similar ($r > .7$) activity were assumed to originate from the same cell, and thus were combined or not included (if one was less stable than the other over the imaging period).

The fluorescence traces from the resulting ROIs of soma (PYRs, VIPs, SSTs) or axons (from ACa) were converted to delta-F through a regression-based smoothing approach (1-s lowess envelope).[63] The first discrete derivative was calculated as a proxy for neuronal activity. Delta-f was z-scored within each neuron using the bottom 8% of signals across each run and then averaged across trials for each stimulus type. Only "visually responsive" cells, i.e., cells showing >1 standard deviation from average response over baseline to at least one stimulus (out of 4 orientations: 0, 90, 45, 135 deg) under at least one condition (control, redundant, deviant), were considered for analysis.[4,33] If a neuron/axonal-segment showed significant activity to more than one oriented stimulus, we plotted and used only one (the strongest after averaging across contexts for that stimulus) for statistical tests.[4]

For imaging cells during optostimulation, a slightly different quantification was used after the ROI extraction. Frames during which the opto-stimulus was delivered were identified by the presence of saturation artifacts in the imaging dataset. The saturation frame and those immediately before and after were discarded from further analyses (1.07 s). In

contrast to the scoring of neural activity during the oddball paradigm (above), we were unable to quantify fast transient onsets in these experiments (because they started during the opto-artifact). We utilized the slower decay time of the GCaMP6s calcium transients in the time period immediately following the opto-stimulation train. We quantified the average fluorescence value in the 1-s after stimulation and subtracted the eighth percentile of fluorescence in the 5 s occurring prior to the opto-stimulus (the baseline), and then divided the result by this baseline (deltaF/F).[65,66] These responses of V1 neurons were averaged across 7–10 trials within each stimulation condition.

For analyzing cell-level responses during the oddball paradigm, calcium imaging analyses were limited to the 10 trials in each condition (control, redundant, deviant) as described above (due to locomotion and field-of-view drift artifacts). We generated stimulus-triggered averages for each neuron recorded for each of the three conditions. If a given neuron responded greater than 1.67 standard deviations above the pre-stimulus baseline activity for any one condition and any one of the orientations, we included it in subsequent analyses (between 80% and 98% of neurons imaged). Responses to only 1 oriented stimulus for each neuron (the strongest after averaging across contexts) were analyzed. We determined significant SSA and DD at the population-level within each cell class (PYRs, VIPs, SSTs, ACa-axons) statistically as described below. Further, for each cell class, we calculated the proportion of cells showing “true DD”: i.e., response to deviant is largest and is more than 1.67 standard deviations larger than response to control stimulus in two separate sets of trials (5 even vs. 5 odd trials). For analyzing DD and SSA as a function of a cell’s orientation selectivity index (OSI) and selectivity relative to the orientation of the test stimulus, we quantified OSI as 1-circular variance[67,68] on the control trials not used for the main analysis (i.e., the 10–15 trials for each of 8 orientations prior to the final 10). Cells with greater than 0.2 OSI were considered selective. Preferred orientation for each cell was estimated as the phase of the average vector, generated by averaging all responses to the 8 different orientations.

For the optostimulation experiments, we used only runs without significant locomotion/movement artifact, including 7 to 10 trials per stimulation condition (weak, strong-block, 2-Hz, 6-Hz, 10-Hz, 20-Hz, 40-Hz). Average delta-f in the 1 s period after the LED was turned off, averaged across trials within each condition, was used for statistical analyses (see below). Each cell was an observation, and PYRs, VIPs, and SSTs were included as separate groups in a frequencyXcell-class ANOVA to determine whether significant effects of ACa stimulation frequency were present that differed across cell class. Additionally, we carried out an LED-only control condition in two mice, measuring PYR responses in L2/3 to the LED drive in blocks or different frequencies (Figure S6).

K-means clustering analysis of optostimulation responses—Responses of V1 neurons were averaged across 7–10 trials within each stimulation condition and combined regardless of cell class into a cell X stimulation condition matrix (except weak, which showed very low responses for most cells and was excluded from the k-means analysis). This 845 × 6 matrix was reduced to 845 × 5 with a principal components analysis (based on a scree-plot). We then carried out 1000 k-means analyses on real data and on shuffled data (shuffled within cells, across PC dimensions) for k = 2–15 (k = number of clusters). At each

iteration, we quantified the median "within-cluster distance from centroids" to determine the quality of the clustering solution. We averaged these values for each value of k, creating a "scree" plot which shows how much each additional cluster adds to the solution. The point at which this curve becomes linear and parallel with the shuffled data suggests that additional clusters are no longer necessary. This analysis supported the presence of 6 stimulation clusters. We took the average centroid locations across these 6 clusters (on the non-standardized, raw data) and computed their average responses to each ACa-stimulation condition. We plotted for each cluster the proportion of SSTs, VIPs, and PYRs relative to the overall proportion of these cells in the overall dataset. We specifically tested whether the 10 Hz condition differed from the block stimulation for each cluster with a paired t test on the cells in the cluster of interest (two-tails).

Decoding of stimulus orientation from calcium activity—Activity of all ACa-axons or V1-PYRs recorded from 200ms pre-onset to 200ms post-stimulus offset across the first 10 presentations of 90-degree vs. 0-degree stimuli across control, redundant, and deviant contexts were first subjected to principal components analysis (PCA). Scree-plots supported study of the first 6 components. Component scores from this PCA were plotted for each timepoint for each trial for each context for the first 3 components for visual inspection (Figure S4). For analysis, these component weights were then applied to the average responses across the first 84ms (3 frames) for each trial to yield a trial X PC matrix of 10×6 for each stimulus orientation (0° or 90°) and context (control, redundant, deviant). Then, a canonical discriminant analysis (IBM SPSS Statistics for Windows, version XX (IBM Corp., Armonk, N.Y., USA)) was conducted separately for each context, adding all 6 components in the analysis together to derive a single canonical discriminant function which was tested for decoding significance as a Chi-square statistic. Further, we employed a "leave one out" cross-validation procedure for each condition.

Local field potential signal processing and analysis—Trials with excessive signal (>≈5 std devs) in either V1 and ACa were manually excluded (between 0 and 20). All analyses were limited to the last 10 control trials and the first 10 deviants of each orientation (two per mouse). We used the 4^{th} redundant in each sequence after each deviant (also 10 total for each orientation). Analyses were combined across both orientations, as local field potential responses in mouse V1 are known to not exhibit significant orientation selectivity.[69] Trial-averaged evoked responses to a given stimulus in the control, redundant, and deviant contexts were generated for each mouse and averaged over mice (Figure 1) for descriptive purposes only. Ongoing data were converted to the time-frequency domain with a modified morelet wavelet approach with 100 evenly spaced wavelets from 1 to 120Hz, linearly increasing in length from 1 to 20 cycles per wavelet, applied every 10ms from 300ms pre-to 700ms post stimulus onset (200ms post-stimulus offset) as previously described.[2] Stimulus-induced power spectra (1–120 Hz) were computed for all three conditions (control, redundant, deviant) for each mouse and baseline-corrected by subtracting the average for each frequency in the 100ms prior to stimulus onset. Statistical analyses focused on identifying signatures of DD (deviant vs. control) in the low-theta band induced power and phase locking during the stimulus period, as this band has been previously shown to track DD in rodents and humans.[2,38,70,71]

Interregional phase synchrony was quantified by taking the phase difference for each frequency (1–40 Hz) between ACa and V1 for all measurements from 100 ms pre-to 100ms post-stimulus offset (separately for control, redundant, and deviant trials) and calculating the 1-circular variance (R-statistic) of these lags. We averaged these values and compared them to the random distribution at $p < .05$.[28,72]

Granger analysis—For analyzing the directionality of interregional connectivity, we carried out two approaches. First, we calculated non-parametric Granger causality, based on past work[30,31] and as implemented in the Fieldtrip toolbox.[73] This analysis examined lagged spectral covariance between regions for each direction (ACa to future-V1 vs. V1 to future-ACa) for each frequency 1-120Hz.

Next, because it is possible that our rapid paradigm (presenting stimuli at 1.1Hz) might not give enough time for dynamic changes in low-frequencies that are specific to the current stimulus (which is only present for 500ms), we carried out a second approach, focusing on how local activity in one region might be predicted by past low-frequency phase in the other region: long-range phase-amplitude coupling (PAC). As a proxy for local activity, we focused on high gamma-power (70–120 Hz) because i) changes in this power envelope in sensory cortical processing are more dynamic than changes in lower frequencies, and ii) high gamma reflects synchronous, highly local neuronal activity.[21,40]

After converting data to the time-frequency domain via Morelet wavelets (see Local field potential signal processing and analysis above), we specifically assessed how phases of oscillations from 3 to 39Hz in one region (ACa or V1) modulated the power of oscillations from 40 to 120Hz in another region (V1 or ACa) at a physiologically plausible future timepoint (i.e., 10ms in the future, see below). We quantified the magnitude of this effect relative to ongoing flux of oscillatory power by employing a Granger framework, using a regression-based approach.[74] For each frequency (in 1-Hz steps), power in region A at timepoint “t” was treated as a criterion variable Y, and was first regressed on power in the same region (region A) at the same frequency at timepoint “t minus lag” (X1). Then, the phase in region B at timepoint “t minus lag” was added to the model as two variables (imaginary and real components of the phasor, X2 and X3) for frequencies 3 to 39Hz. The change in R^2 in this new model (including X1,X2,X3) compared to the original model (including just X1) was quantified as an F-value–the so-called “long-range PAC coefficient”. These PAC coefficients were quantified combining data from all trials and all timepoints from 100 pre-stimulus to 100ms post-stimulus offset, separately for each directions (ACa-phase to V1-power [“top-down”] and V1-phase to ACa-power [“bottom-up”]) and for each frequency pair in the respective windows (3-39Hz, and 40-120Hz) and for each mouse and trial type (control, redundant, deviant). Results were first log-transformed and averaged over all mice and trial-types to yield a single global long-range PAC spectra for each direction (top-down and bottom-up), which were then compared to identify key regions of peak long-range PAC (Figure 2E).

For both analyses (typical Granger and long-range PAC Granger), we focused on a time-lag of 10ms given i) that similar studies of long-range brain connectivity show similar lags[75] and ii) the lag of antidromic activation we identified in our optogenetic stimulation

experiments (Figure S5E). For statistical analyses of different traditional long-range PAC values (Figures 2G and 2H; S2C and S2D), we used 70-120Hz as the gamma-power envelope for the high- "modulated" frequency, but slightly different frequencies for each mouse for the low- "modulating/phase" frequency. We identified peak-frequency the strongest interregional synchrony (between ACa and V1) within a given "low-frequency" band: theta/alpha (4-14Hz; Figures 2G and 2H), low-beta (15-20Hz), and high-beta (25-30Hz). These bands were chosen based on the peaks in the heatmap from Figures 2E and 2F, which were collapsed across all trials and thus could not bias our subsequent trial-wise comparisons.

Behavior and locomotion detection—Videos of mice during experiments were recorded at 30 fps during each experiment via a Logitech C920 HD Pro webcam mounted ≈20 cm away from the mouse's face, illuminated by a dim 617 nm LED. Wheel motion, a surrogate of mouse locomotion, nose and whisker movement were calculated on a frame by frame basis post-hoc by singular value decomposition of manually selected ROIs using the open-source Facemap software.[76] Stimulus traces were aligned to the onset of the stimulus in each video. Behavioral variables were standardized relative to the peak value for each recording and analyzed similarly to LFP data, as stimulus-triggered averages C (control), R (redundant), and D (deviant; Figure S1).

Statistics—For calcium imaging experiments, we carried out repeated-measures or factorial ANOVAs on the measures of interest at the cell-level with STIMULUS TYPE (control, redundant, deviant) or STIMULATION FREQUENCY (block, 2-, 6-, 10-, 20-, or 40-Hz) as within-subjects factors. Significant effects were carried out with t-tests (two-tailed), focusing on planned contrasts between i) control and redundants (which tests for "SSA") and ii) controls and deviants (which tests for "DD") as previously described. For comparisons within selective or non-selective subgroups (Figure 4), one-tailed t-tests were used when the direction of the effects was hypothesized *a priori* (i.e., for PYR DD and SSA). For LFP experiments, we carried out repeated-measures or mixed-ANOVAs on the measures of interest at the mouse level (one measurement per mouse) with STIMULUS TYPE (control, redundant, deviant) and/or CNO- (pre, post) as within-subjects factors and GROUP (hM4D(i), controls) as a between-subjects factor. Significant interactions were carried out with t-tests (two-tailed).

Supplementary Material

Refer to Web version on PubMed Central for supplementary material.

ACKNOWLEDGMENTS

This work was funded by the National Eye Institute (R01EY033950 to J.P.H.), the National Institute of Mental Health (K99/R00MH115082 to J.P.H. and F32MH125445 to J.M.R.), the National Institute of General Medical Sciences (5T34GM131939), the Brain and Behavior Research Foundation (YI30149 to J.P.H.), and the Whitehall Foundation (2019-05-443 to J.P.H.).

INCLUSION AND DIVERSITY

One or more of the authors of this paper self-identifies as a member of the LGBTQIA+ community. One or more of the authors of this paper received support from a program designed to increase minority representation in their field of research. We support inclusive, diverse, and equitable conduct of research.

REFERENCES

1. Gilbert C, Ito M, Kapadia M, and Westheimer G (2000). Interactions between attention, context and learning in primary visual cortex. Vision Res. 40, 1217–1226. 10.1016/s0042-6989(99)00234-5. [PubMed: 10788637]
2. Hamm JP, and Yuste R (2016). Somatostatin Interneurons Control a Key Component of Mismatch Negativity in Mouse Visual Cortex. Cell Rep. 16, 597–604. 10.1016/j.celrep.2016.06.037. [PubMed: 27396334]
3. Kremláček J, Kreegipuu K, Tales A, Astikainen P, Põldver N, Näätänen R, and Stefanics G (2016). Visual mismatch negativity (vMMN): A review and meta-analysis of studies in psychiatric and neurological disorders. Cortex 80, 76–112. 10.1016/j.cortex.2016.03.017. [PubMed: 27174389]
4. Hamm JP, Shymkiv Y, Han S, Yang W, and Yuste R (2021). Cortical ensembles selective for context. Proc. Natl. Acad. Sci 118, e2026179118. 10.1073/pnas.2026179118. [PubMed: 33811144]
5. Friston K. (2005). A theory of cortical responses. Philos. Trans. R. Soc. Lond. B Biol. Sci 360, 815–836. 10.1098/rstb.2005.1622. [PubMed: 15937014]
6. Gallimore CG, Ricci DA, and Hamm JP (2023). Spatiotemporal dynamics across visual cortical laminae support a predictive coding framework for interpreting mismatch responses. Cereb. Cortex 33, 9417–9428, 1991, bhad215.. 10.1093/cercor/bhad215 [PubMed: 37310190]
7. Bastos AM, Usrey WM, Adams RA, Mangun GR, Fries P, and Friston KJ (2012). Canonical Microcircuits for Predictive Coding. Neuron 76, 695–711. 10.1016/j.neuron.2012.10.038. [PubMed: 23177956]
8. Jordan R, and Keller GB (2020). Opposing Influence of Top-down and Bottom-up Input on Excitatory Layer 2/3 Neurons in Mouse Primary Visual Cortex. Neuron 108, 1194–1206.e5. 10.1016/J.NEURON.2020.09.024. [PubMed: 33091338]
9. Tremblay R, Lee S, and Rudy B (2016). GABAergic Interneurons in the Neocortex: From Cellular Properties to Circuits. Neuron 91, 260–292. 10.1016/j.neuron.2016.06.033. [PubMed: 27477017]
10. Keller AJ, Dipoppa M, Roth MM, Caudill MS, Ingrosso A, Miller KD, and Scanziani M (2020). A Disinhibitory Circuit for Contextual Modulation in Primary Visual Cortex. Neuron 108, 1181–1193.e8. 10.1016/j.neuron.2020.11.013. [PubMed: 33301712]
11. Buzsáki G, and Chrobak JJ (1995). Temporal structure in spatially organized neuronal ensembles: a role for interneuronal networks. Curr. Opin. Neurobiol 5, 504–510. 10.1016/0959-4388(95)80012-3. [PubMed: 7488853]
12. Markram H, Toledo-Rodriguez M, Wang Y, Gupta A, Silberberg G, and Wu C (2004). Interneurons of the neocortical inhibitory system. Nat. Rev. Neurosci 5, 793–807. 10.1038/nrn1519. [PubMed: 15378039]
13. Lee S-H, Kwan AC, Zhang S, Phoumthipphavong V, Flannery JG, Masmanidis SC, Taniguchi H, Huang ZJ, Zhang F, Boyden ES, et al. (2012). Activation of specific interneurons improves V1 feature selectivity and visual perception. Nature 488, 379–383. 10.1038/nature11312. [PubMed: 22878719]
14. Pfeffer CK, Xue M, He M, Huang ZJ, and Scanziani M (2013). Inhibition of inhibition in visual cortex: the logic of connections between molecularly distinct interneurons. Nat. Neurosci 16, 1068–1076. 10.1038/nn.3446. [PubMed: 23817549]
15. Karnani MM, Jackson J, Ayzenshtat I, Tucciarone J, Manoocheri K, Snider WG, and Yuste R (2016). Cooperative Subnetworks of Molecularly Similar Interneurons in Mouse Neocortex. Neuron 90, 86–100. 10.1016/j.neuron.2016.02.037. [PubMed: 27021171]

16. Ross JM, and Hamm JP (2020). Cortical Microcircuit Mechanisms of Mismatch Negativity and Its Underlying Subcomponents. Front. Neural Circuits 14, 13–15. 10.3389/fncir.2020.00013. [PubMed: 32296311]
17. Zhang S, Xu M, Kamigaki T, Hoang Do JP, Chang W-C, Jenvay S, Miyamichi K, Luo L, and Dan Y (2014). Selective attention. Long-range and local circuits for top-down modulation of visual cortex processing. Science 345, 660–665. 10.1126/science.1254126. [PubMed: 25104383]
18. Norman KJ, Riceberg JS, Koike H, Bateh J, McCraney SE, Caro K, Kato D, Liang A, Yamamuro K, Flanigan ME, et al. (2021). Post-error recruitment of frontal sensory cortical projections promotes attention in mice. Neuron 109, 1202–1213.e5. 10.1016/j.neuron.2021.02.001. [PubMed: 33609483]
19. Pi H-J, Hangya B, Kvitsiani D, Sanders JI, Huang ZJ, and Kepecs A (2013). Cortical interneurons that specialize in disinhibitory control. Nature 503, 521–524. 10.1038/nature12676. [PubMed: 24097352]
20. Kamigaki T. (2019). Dissecting executive control circuits with neuron types. Neurosci. Res 141, 13–22. 10.1016/j.neures.2018.07.004. [PubMed: 30110598]
21. Buzsáki G, and Wang X-J (2012). Mechanisms of Gamma Oscillations. Annu. Rev. Neurosci 35, 203–225. 10.1146/annurev-neuro-062111-150444. [PubMed: 22443509]
22. Uhlhaas PJ, and Singer W (2010). Abnormal neural oscillations and synchrony in schizophrenia. Nat. Rev. Neurosci 11, 100–113. 10.1038/nrn2774. [PubMed: 20087360]
23. Hong LE, Buchanan RW, Thaker GK, Shepard PD, and Summerfelt A (2008). Beta (~16 Hz) frequency neural oscillations mediate auditory sensory gating in humans. Psychophysiology 45, 197–204. 10.1111/j.1469-8986.2007.00624.x. [PubMed: 17995907]
24. HajiHosseini A, Rodríguez-Fornells A, and Marco-Pallarés J (2012). The role of beta-gamma oscillations in unexpected rewards processing. Neuroimage 60, 1678–1685. 10.1016/J.NEUROIMAGE.2012.01.125. [PubMed: 22330314]
25. Herweg NA, Solomon EA, and Kahana MJ (2020). Theta oscillations in human memory. Trends Cogn. Sci 24, 208–227. 10.1016/J.TICS.2019.12.006. [PubMed: 32029359]
26. Schmiedt C, Brand A, Hildebrandt H, and Basar-Eroglu C (2005). Event-related theta oscillations during working memory tasks in patients with schizophrenia and healthy controls. Cogn. Brain Res 25, 936–947. 10.1016/J.COGBRAINRES.2005.09.015.
27. Abbas AI, Sundiang MJM, Henoch B, Morton MP, Bolkan SS, Park AJ, Harris AZ, Kellendonk C, and Gordon JA (2018). Somatostatin Interneurons Facilitate Hippocampal-Prefrontal Synchrony and Prefrontal Spatial Encoding. Neuron 100, 926–939.e3. 10.1016/j.neuron.2018.09.029. [PubMed: 30318409]
28. Hamm JP, Dyckman KA, McDowell JE, and Clementz BA (2012). Pre-cue fronto-occipital alpha phase and distributed cortical oscillations predict failures of cognitive control. J. Neurosci 32, 7034–7041. 10.1523/JNEUROSCI.5198-11.2012. [PubMed: 22593071]
29. Buzsaki G. (2009). Rhythms of the Brain (Oxford University Press).
30. Bastos AM, Lundqvist M, Waite AS, Kopell N, and Miller EK (2020). Layer and rhythm specificity for predictive routing. Proc. Natl. Acad. Sci. USA 117, 31459–31469. 10.1073/pnas.2014868117. [PubMed: 33229572]
31. Bastos AM, Vezoli J, Bosman CA, Schoffelen JM, Oostenveld R, Dowdall JR, DeWeerd P, Kennedy H, and Fries P (2015). Visual areas exert feedforward and feedback influences through distinct frequency channels. Neuron 85, 390–401. 10.1016/j.neuron.2014.12.018. [PubMed: 25556836]
32. Lee M, Sehatpour P, Hoptman MJ, Lakatos P, Dias EC, Kantrowitz JT, Martinez AM, and Javitt DC (2017). Neural mechanisms of mismatch negativity dysfunction in schizophrenia. Mol. Psychiatry 22, 1585–1593. 10.1038/mp.2017.3. [PubMed: 28167837]
33. Van Derveer AB, Ross JM, and Hamm JP (2023). Robust multisensory deviance detection in the mouse parietal associative area. Curr. Bio 10.1016/j.cub.2023.08.002.
34. Zhang S, Xu M, Chang W-C, Ma C, Hoang Do JP, Jeong D, Lei T, Fan JL, and Dan Y (2016). Organization of long-range inputs and outputs of frontal cortex for top-down control. Nat. Neurosci 19, 1733–1742. 10.1038/nn.4417. [PubMed: 27749828]

35. Niell CM, and Stryker MP (2010). Modulation of visual responses by behavioral state in mouse visual cortex. Neuron 65, 472–479. 10.1016/j.neuron.2010.01.033. [PubMed: 20188652]
36. Bimbard C, Sit TPH, Lebedeva A, Reddy CB, Harris KD, and Carandini M (2023). Behavioral origin of sound-evoked activity in mouse visual cortex. Nat. Neurosci 26, 251–258. 10.1038/s41593-022-01227-x. [PubMed: 36624279]
37. Szadai Z, Pi H-J, Chevy Q, Ócsai K, Albeanu DF, Chiovini B, Szalay G, Katona G, Kepecs A, and Rózsa B (2022). Cortex-wide response mode of VIP-expressing inhibitory neurons by reward and punishment. Elife 11, e78815. 10.7554/eLife.78815. [PubMed: 36416886]
38. Javitt DC, Lee M, Kantrowitz JT, and Martinez A (2018). Mismatch negativity as a biomarker of theta band oscillatory dysfunction in schizophrenia. Schizophr. Res 191, 51–60. 10.1016/j.schres.2017.06.023. [PubMed: 28666633]
39. Uhlhaas PJ, Pipa G, Neuenschwander S, Wibral M, and Singer W (2011). A new look at gamma? High- (>60 Hz) γ-band activity in cortical networks: function, mechanisms and impairment. Prog. Biophys. Mol. Biol 105, 14–28. 10.1016/j.pbiomolbio.2010.10.004. [PubMed: 21034768]
40. Logothetis NK, Pauls J, Augath M, Trinath T, and Oeltermann a (2001). Neurophysiological investigation of the basis of the fMRI signal. Nature 412, 150–157. 10.1038/35084005. [PubMed: 11449264]
41. Friston K. (2003). Learning and inference in the brain. Neural Netw. 16, 1325–1352. 10.1016/j.neunet.2003.06.005. [PubMed: 14622888]
42. Friston K, Kilner J, and Harrison L (2006). A free energy principle for the brain. J. Physiol. Paris 100, 70–87. 10.1016/j.jphysparis.2006.10.001. [PubMed: 17097864]
43. Friston K. (2018). Does predictive coding have a future? Nat. Neurosci 21, 1019–1021. 10.1038/s41593-018-0200-7. [PubMed: 30038278]
44. Mumford D. (1992). On the computational architecture of the neocortex. II. The role of cortico-cortical loops. Biol. Cybern 66, 241–251. 10.1007/BF00198477. [PubMed: 1540675]
45. Rao RP, and Ballard DH (1999). Predictive coding in the visual cortex: a functional interpretation of some extra-classical receptive-field effects. Nat. Neurosci 2, 79–87. 10.1038/4580. [PubMed: 10195184]
46. Chen I-W, Helmchen F, and Lütcke H (2015). Specific Early and Late Oddball-Evoked Responses in Excitatory and Inhibitory Neurons of Mouse Auditory Cortex. J. Neurosci 35, 12560–12573. 10.1523/JNEUROSCI.2240-15.2015. [PubMed: 26354921]
47. Parras GG, Nieto-Diego J, Carbajal GV, Valdés-Baizabal C, Escera C, and Malmierca MS (2017). Neurons along the auditory pathway exhibit a hierarchical organization of prediction error. Nat. Commun 8, 2148. 10.1038/s41467-017-02038-6. [PubMed: 29247159]
48. Stefanics G, Kremláček J, and Czigler I (2014). Visual mismatch negativity: a predictive coding view. Front. Hum. Neurosci 8, 666. 10.3389/fnhum.2014.00666. [PubMed: 25278859]
49. Sammari M, Inglebert Y, Ankri N, Russier M, Incontro S, and Debanne D (2022). Theta patterns of stimulation induce synaptic and intrinsic potentiation in O-LM interneurons. Proc. Natl. Acad. Sci 119, e2205264119. 10.1073/pnas.2205264119. [PubMed: 36282913]
50. Karnani MM, Jackson J, Ayzenshtat I, Hamzehei Sichani A, Manoocheri K, Kim S, and Yuste R (2016). Opening Holes in the Blanket of Inhibition: Localized Lateral Disinhibition by VIP Interneurons. J. Neurosci 36, 3471–3480. 10.1523/JNEUROSCI.3646-15.2016. [PubMed: 27013676]
51. Heintz TG, Hinojosa AJ, Dominiak SE, and Lagnado L (2022). Opposite forms of adaptation in mouse visual cortex are controlled by distinct inhibitory microcircuits. Nat. Commun 13, 1031. 10.1038/s41467-022-28635-8. [PubMed: 35210417]
52. Jiang X, Shen S, Cadwell CR, Berens P, Sinz F, Ecker AS, Patel S, and Tolias AS (2015). Principles of connectivity among morphologically defined cell types in adult neocortex. Science 350, aac9462, 1–9. 10.1126/science.aac9462.
53. Apicella AJ, and Marchionni I (2022). VIP-Expressing GABAergic Neurons: Disinhibitory vs. Inhibitory Motif and Its Role in Communication Across Neocortical Areas. Front. Cell. Neurosci 16, 811484. 10.3389/fncel.2022.811484. [PubMed: 35221922]

54. Karnani MM, Agetsuma M, and Yuste R (2014). A blanket of inhibition: functional inferences from dense inhibitory connectivity. Curr. Opin. Neurobiol 26, 96–102. 10.1016/j.conb.2013.12.015. [PubMed: 24440415]
55. Millman DJ, Ocker GK, Caldejon S, Kato I, Larkin JD, Lee EK, Luviano J, Nayan C, Nguyen TV, North K, et al. (2020). VIP interneurons in mouse primary visual cortex selectively enhance responses to weak but specific stimuli. Elife 9, e55130. 10.7554/eLife.55130. [PubMed: 33108272]
56. Garrett M, Manavi S, Roll K, Ollerenshaw DR, Groblewski PA, Ponvert ND, Kiggins JT, Casal L, Mace K, Williford A, et al. (2020). Experience shapes activity dynamics and stimulus coding of VIP inhibitory cells. Elife 9, e50340. 10.7554/eLife.50340. [PubMed: 32101169]
57. Light GA, and Näätänen R (2013). Mismatch negativity is a break-through biomarker for understanding and treating psychotic disorders. Proc. Natl. Acad. Sci. USA 110, 15175–15176. 10.1073/pnas.1313287110. [PubMed: 23995447]
58. Garrett M, Groblewski P, Piet A, Ollerenshaw D, Najafi F, Yavorska I, Amster A, Bennett C, Buice M, Caldejon S, et al. (2023). Stimulus novelty uncovers coding diversity in visual cortical circuits. Preprint at bioRxiv. 10.1101/2023.02.14.528085.
59. Harms L, Michie PT, and Näätänen R (2016). Criteria for determining whether mismatch responses exist in animal models: Focus on rodents. Biol. Psychol 116, 28–35. 10.1016/j.biopsycho.2015.07.006. [PubMed: 26196895]
60. Kaser M, Soltesz F, Lawrence P, Miller S, Dodds C, Croft R, Dudas RB, Zaman R, Fernandez-Egea E, Müller U, et al. (2013). Oscillatory underpinnings of mismatch negativity and their relationship with cognitive function in patients with schizophrenia. PLoS One 8, e83255. 10.1371/journal.pone.0083255. [PubMed: 24358266]
61. Bastos G, Holmes JT, Ross JM, Rader AM, Gallimore CG, Wargo JA, Peterka DS, and Hamm JP (2023). Calcium imaging, LFP, and behavioral data for Top-down input modulates visual context processing through an interneuron-specific circuit. 10.5281/zenodo.8273225.
62. Bastos G, Holmes JT, Ross JM, Rader AM, Gallimore CG, Wargo JA, Peterka DS, Hamm JP Code for Top-down input modulates visual context processing through an interneuron-specific circuit. 2023. 10.5281/zenodo.8335415
63. Hamm JP, Peterka DS, Gogos JA, and Yuste R (2017). Altered Cortical Ensembles in Mouse Models of Schizophrenia. Neuron 94, 153–167.e8. 10.1016/j.neuron.2017.03.019. [PubMed: 28384469]
64. Dubbs A, Guevara J, and Yuste R (2016). moco: Fast Motion Correction for Calcium Imaging. Front. Neuroinform 10, 6. 10.3389/fninf.2016.00006. [PubMed: 26909035]
65. Miller J. -e. K., Ayzenshtat I, Carrillo-Reid L, and Yuste R (2014). Visual stimuli recruit intrinsically generated cortical ensembles. Proc. Natl. Acad. Sci 111, E4053–E4061. 10.1073/pnas.1406077111. [PubMed: 25201983]
66. Chen TW, Wardill TJ, Sun Y, Pulver SR, Renninger SL, Baohan A, Schreiter ER, Kerr RA, Orger MB, Jayaraman V, et al. (2013). Ultrasensitive fluorescent proteins for imaging neuronal activity. Nature 499, 295–300. 10.1038/nature12354. [PubMed: 23868258]
67. Mazurek M, Kager M, and Van Hooser SD (2014). Robust quantification of orientation selectivity and direction selectivity. Front. Neural Circuits 8, 92–17. 10.3389/fncir.2014.00092. [PubMed: 25147504]
68. Hamm JP, Shymkiv Y, Mukai J, Gogos JA, and Yuste R (2020). Aberrant Cortical Ensembles and Schizophrenia-like Sensory Phenotypes in Setd1a+/− Mice. Biol. Psychiatry 88, 215–223. 10.1016/j.biopsych.2020.01.004. [PubMed: 32143831]
69. Land R, Engler G, Kral A, and Engel AK (2013). Response properties of local field potentials and multiunit activity in the mouse visual cortex. Neuroscience 254, 141–151. 10.1016/j.neuroscience.2013.08.065. [PubMed: 24035827]
70. Lee M, Balla A, Sershen H, Sehatpour P, Lakatos P, and Javitt DC (2018). Rodent Mismatch Negativity/theta Neuro-Oscillatory Response as a Translational Neurophysiological Biomarker for N-Methyl-D-Aspartate Receptor-Based New Treatment Development in Schizophrenia. Neuropsychopharmacology 43, 571–582. 10.1038/NPP.2017.176. [PubMed: 28816240]

71. Hamm JP, Ethridge LE, Shapiro JR, Stevens MC, Boutros NN, Summerfelt AT, Keshavan MS, Sweeney JA, Pearlson G, Tamminga CA, et al. (2012). Spatiotemporal and frequency domain analysis of auditory paired stimuli processing in schizophrenia and bipolar disorder with psychosis. Psychophysiology 49, 522–530. 10.1111/j.1469-8986.2011.01327.x. [PubMed: 22176721]

72. Moratti S, Clementz BA, Gao Y, Ortiz T, and Keil A (2007). Neural mechanisms of evoked oscillations: stability and interaction with transient events. Hum. Brain Mapp 28, 1318–1333. 10.1002/hbm.20342. [PubMed: 17274017]

73. Oostenveld R, Fries P, Maris E, and Schoffelen J-M (2011). FieldTrip: Open source software for advanced analysis of MEG, EEG, and invasive electrophysiological data. Comput. Intell. Neurosci 2011, 156869. 10.1155/2011/156869. [PubMed: 21253357]

74. Granger CWJ (1969). Investigating Causal Relations by Econometric Models and Cross-spectral Methods. Econometrica 37, 424–438. 10.2307/1912791.

75. Jackson J, Karnani MM, Zemelman BV, Burdakov D, and Lee AK (2018). Inhibitory Control of Prefrontal Cortex by the Claustrum. Neuron 99, 1029–1039.e4. 10.1016/j.neuron.2018.07.031. [PubMed: 30122374]

76. Stringer C, Pachitariu M, Steinmetz N, Reddy CB, Carandini M, and Harris KD (2019). Spontaneous behaviors drive multidimensional, brain-wide activity. Science 364, 255. 10.1126/science.aav7893. [PubMed: 31000656]

Highlights

- Visual cortex processes stimuli in context, detecting deviant stimuli in predictable sequences
- Prefrontal and visual cortex synchronize at ≈10 Hz during predictable sequences
- Subsets of VIP neurons increase and SSTs decrease activity during predictable sequences
- Inactivation of VIPs disrupts 10-Hz fronto-visual synchrony and visual context processing

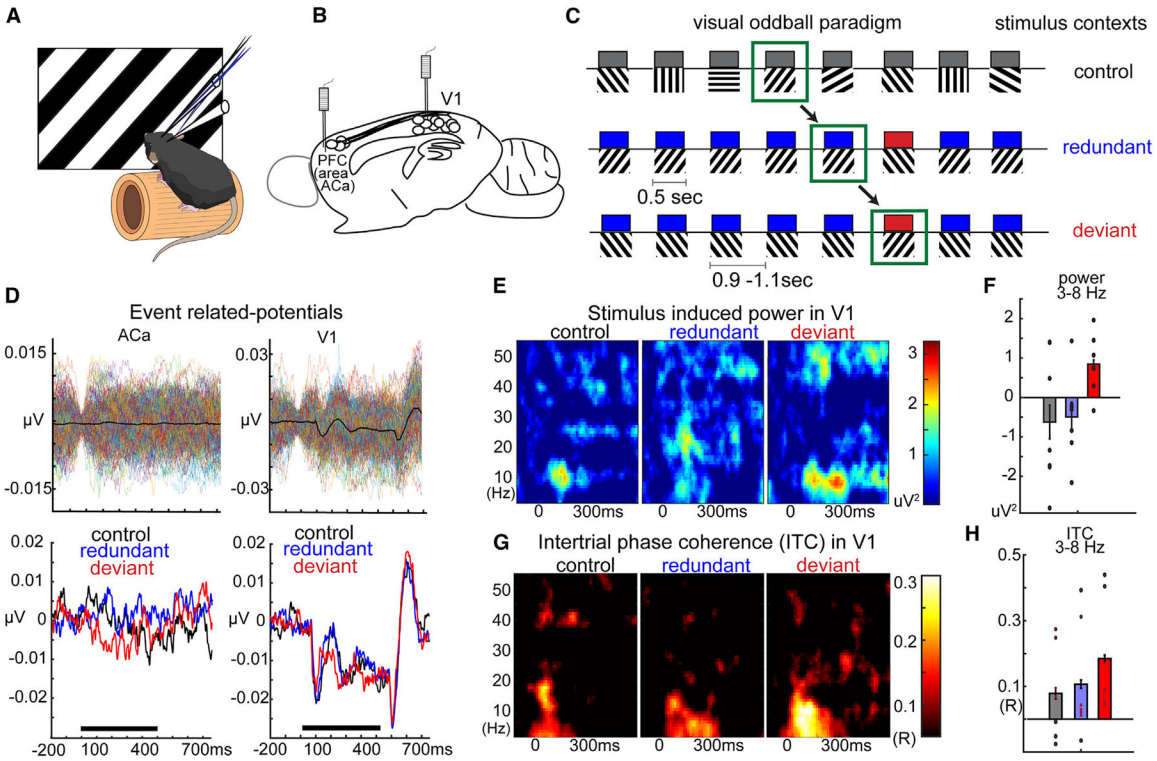

Figure 1. DD in V1 power and phase dynamics in the LFP during a visual oddball paradigm

(A and B) Awake mice viewed full-field visual gratings (A) during LFP recordings in the (B) V1 cortex and anterior cingulate area (ACa).

(C) Visual stimuli in a standard oddball, oddball flip, and many-standards control paradigm. Visual responses to the same stimulus were tracked in neutral (equiprobable), redundant, and deviant contexts.

(D) Individual trial activity and trial-averaged activity in the Aca and V1 from (top) a single mouse and (bottom) averaged over mice within each stimulus context show that only the V1 displayed clear visually evoked responses to the stimuli.

(E and F) Stimulus-induced power in control, redundant, and deviant contexts evince an increase in theta-band power to the deviant stimulus.

(G and H) Stimulus-evoked inter-trial phase locking (ITC) evince an early latency increase in theta-band ITC.

All error bars reflect within-subjects standard error pooled across mice. See also Figure S1.

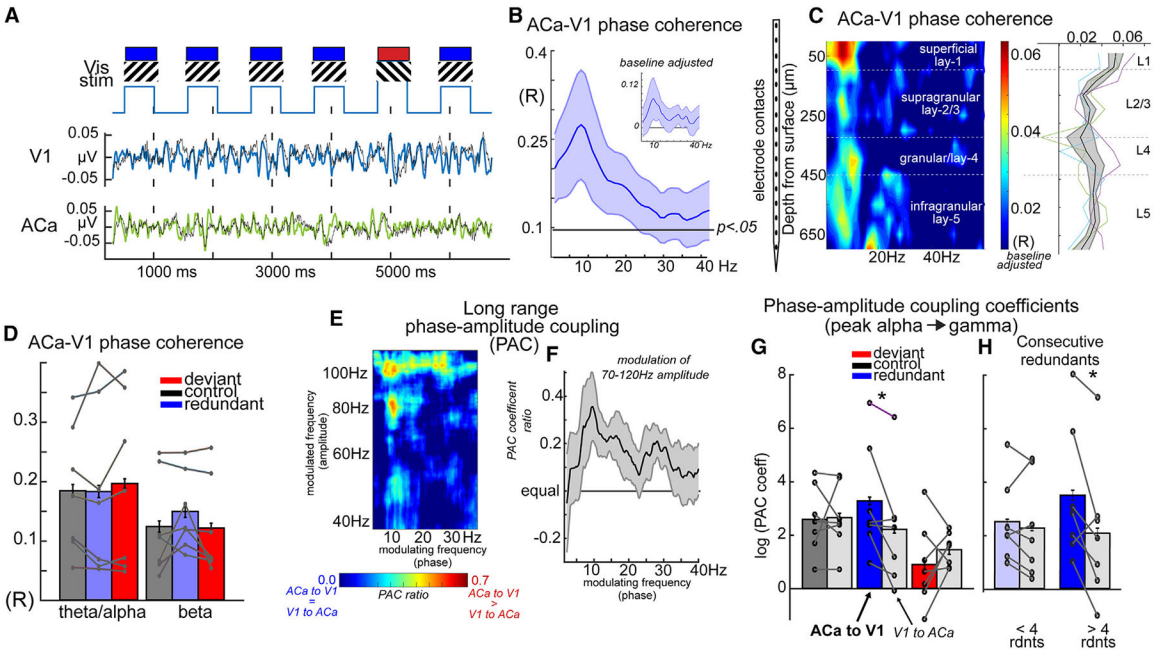

Figure 2. Long range fronto-visual synchrony in the theta/alpha band during the oddball paradigm

(A) Bipolar electrical recordings in the V1 and ACa displayed as ongoing unfiltered (black) and filtered LFPs in the theta/alpha band (8–13 Hz).

(B) Interregional phase synchrony (R-statistic) averaged across 7 mice and compared with randomized values at $p < 0.05$. Inset: subtracting pre-stimulus phase synchrony.

(C) Recordings of a single ACa electrode combined with a multielectrode probe (16 channels) in 3 mice, showing that ACa-V1 theta/alpha synchrony is strongest in L1, where ACa axons terminate in the V1.

(D) Interregional phase synchrony did not differ across stimulus types in theta/alpha (8–13 Hz) or beta (15–25 Hz) bands.

(E and F) Long-range lagged-phase amplitude coupling (PAC) across regions, averaged across mice and conditions. ACa low-frequency phase predicted future V1 gamma power (70–120 Hz) stronger than the inverse direction (V1 phase to ACa power) (E), and this peaked at 10 Hz (F).

(G) Bar plots and individual mouse (points) long-range PAC data from the peak region in (F) quantified by stimulus condition evince a stimulus type by direction interaction.

(H) This directional difference was stronger after 4 redundant stimuli post deviant stimuli; *$p < 0.05$, paired-samples t test.

All error bars (D, G, and H) and shaded regions around lines (B, C, and F) reflect within-subjects standard error pooled across mice. See also Figures S1 and S2.

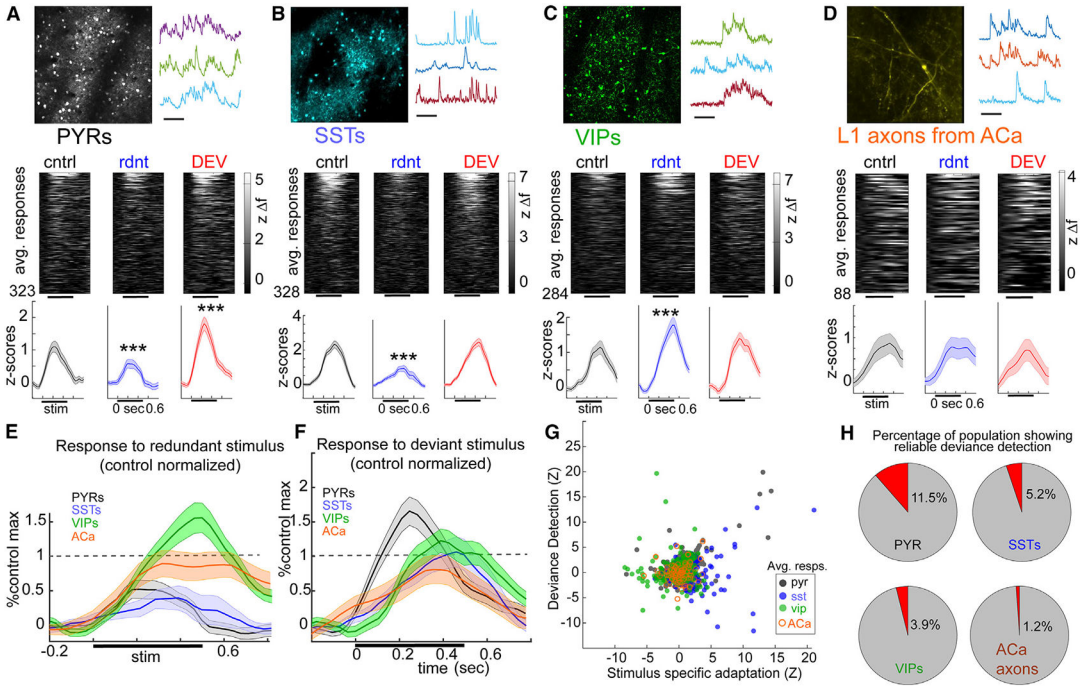

Figure 3. Cell-type-specific dynamics in the V1-ACa circuit during the oddball paradigm

(A) Top: two-photon calcium imaging of pyramidal neurons (PYRs; n = 4 mice; scale bar, 15 s) during a visual oddball paradigm. Center: raster plot of average responses to a stimulus when in control, redundant (fourth in sequence), and deviant contexts (over 10 trials for each; includes 323 visually responsive neurons). Bottom: average responses across neurons show significant SSA (redundant vs. control) and significant DD (deviant vs. control).

(B) Same as (A) for SST+ neurons (n = 8 mice; 328 neurons, 98% of recorded). Bottom: average responses show significant SSA but not DD.

(C) Same as (A) for VIP+ neurons (n = 9 mice; 284 neurons, 93% of recorded). Bottom: average responses show significant inverse SSA but not DD.

(D) Same as (A) for ACa axon segments and boutons (regions of interest [ROIs]) in L1 of the V1 (n = 4 mice; 89 neurons, 89% of recorded). Bottom: average responses show neither significant SSA nor significant DD.

(E) Average responses to the redundant stimulus scaled relative to the maximum average response to the control stimulus within each cell type.

(F) Same as (E) for the deviant stimulus.

(G) Scatterplot showing computed “DD” and “SSA” for each neuron.

(H) Percentage of each cell/ROI type showing reliable DD; ***$p < 0.005$.

All shaded regions around lines reflect standard error pooled across cells. See also Figure S3.

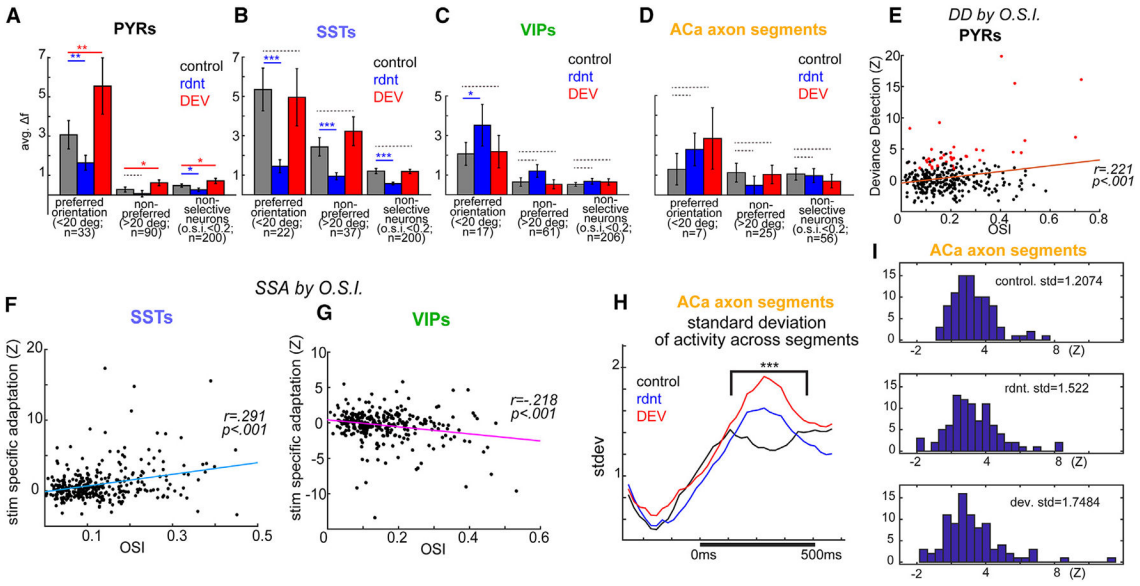

Figure 4. Neuronal subtype dynamics and features during the oddball paradigm

(A–D) Responses of neuronal subtypes to control vs. redundant vs. deviant contexts as a function of their orientation selectivity for the presented stimulus.

(E) DD in PYRs was modestly but significantly correlated with orientation selectivity. Cells showing both low and high orientation selectivity showed reliable DD (red cells in the plot).

(F and G) SSA in SSTs was modestly but significantly correlated with orientation selectivity (F), while SSA in VIPs was inversely correlated with orientation selectivity (G).

(H and I) ACa axons in the V1 exhibit increased standard deviation across population responses during redundant and deviant trials relative to control; *p < 0.05, **p < 0.01, ***p < 0.005.

Error bars in (A)–(D) reflect standard error across cells. See also Figure S4.

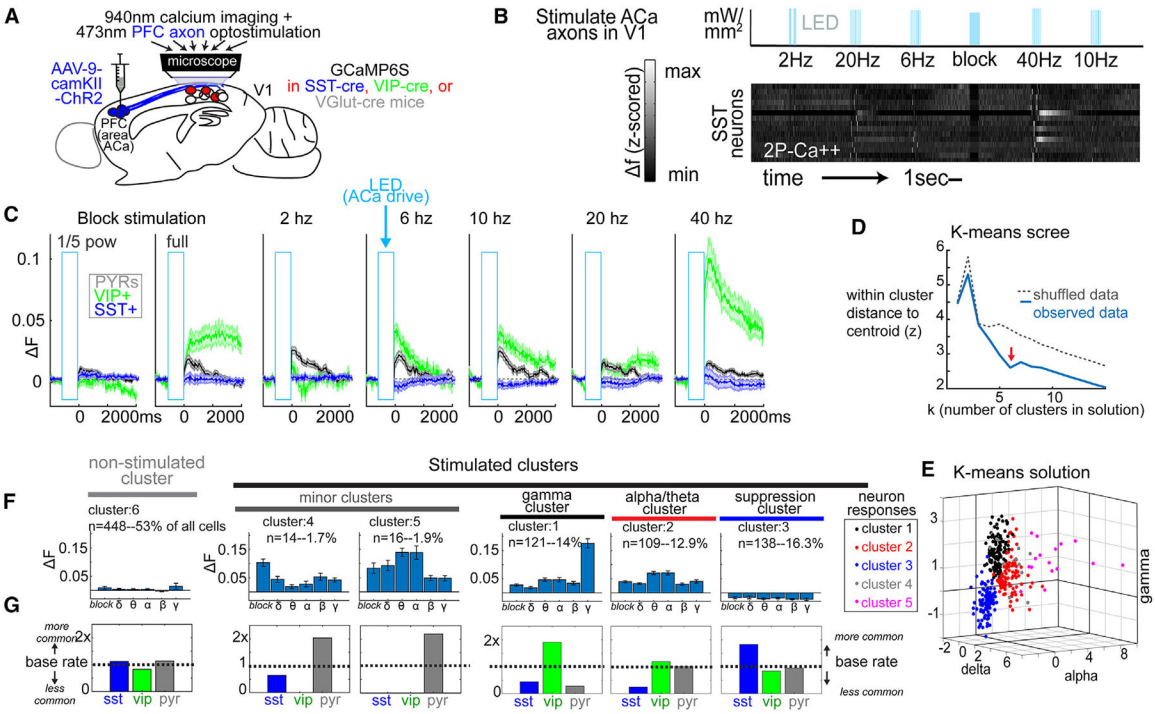

Figure 5. V1 activation by ACa is frequency and cell type specific

(A) ChR2 expressed in the ACa of mice expressing GCaMP6S in PYR, VIP, or SST interneurons.

(B) Activity of PYRs, VIPs, or SSTs was imaged in the V1 while 1-s bursts of 473-nm light illuminated the imaging column to activate ACa axons at 2, 6, 10, 20, or 40 Hz, a power-normalized “weak” block stimulation, and a full-power block stimulation.

(C) During optogenetic driving of ACa inputs, activity differed among VIPs, SSTs, and PYRs in V1.

(D) Cell responses for all stimulation conditions (except weak) were subjected to a series of k-means analyses on shuffled and real data, suggesting the presence of 6 stimulation clusters.

(E) Responses of individual cells plotted in a scatterplot for delta (2 Hz), alpha (10 Hz), and gamma (40 Hz), excluding the cluster with no strong ACa drive (about half of the cells).

(F) Average centroid locations across these 6 clusters to each ACa stimulation condition. This included a non-stimulated cluster and 5 stimulation clusters.

(G) Proportion of SSTs, VIPs, and PYRs relative to the overall proportion of these cells in the overall dataset were plotted for each cluster.

All error bars (F) and shaded regions around lines (C) reflect within-subjects standard error pooled across cells. See also Figures S5 and S6.

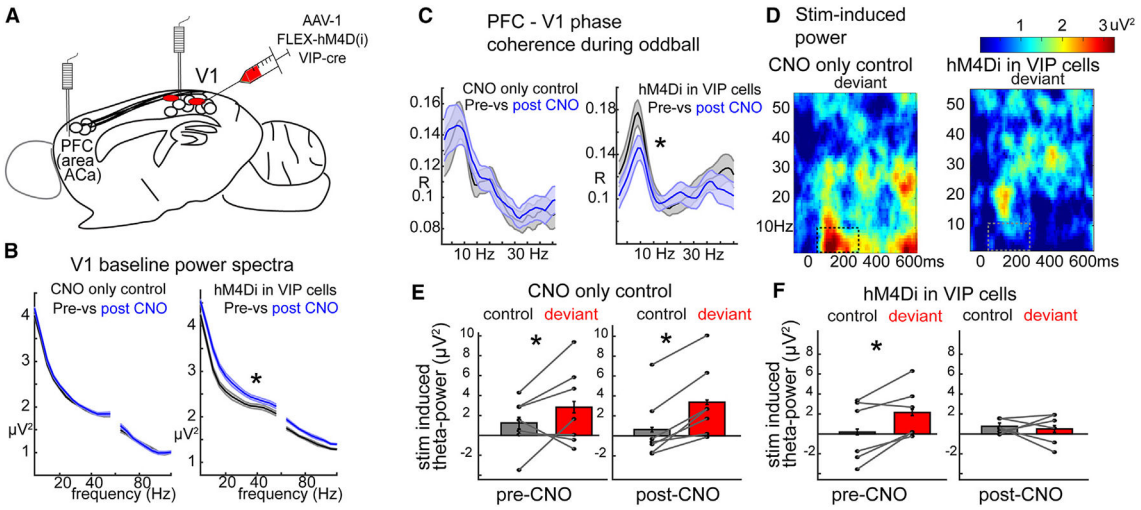

Figure 6. Chemogenetic suppression of VIP neuron activity in the V1 eliminates fronto-visual synchrony and visual DD in the LFP

(A) Inhibitory DREADDs (hM4Di) expressed in VIP+ interneurons in the V1. LFPs were recorded in the ACa and V1.

(B) VIP interneuron suppression increased broadband power at baseline (inter-stimulus intervals).

(C) VIP interneuron suppression decreased interregional phase synchrony during the stimulus period of the oddball paradigm.

(D) Stimulus-induced power spectra to the deviant stimuli post CNO.

(E and F) Stimulus-induced theta-band power from boxes in (D); 3–8 Hz; 50–250 ms post stimulus onset, based on the global average power plot in Figure S7E. Points represent mice (*$p < 0.05$).

All error bars (E and F) and shaded regions around lines (B and C) reflect within-subjects standard error pooled across mice. See also Figure S7.

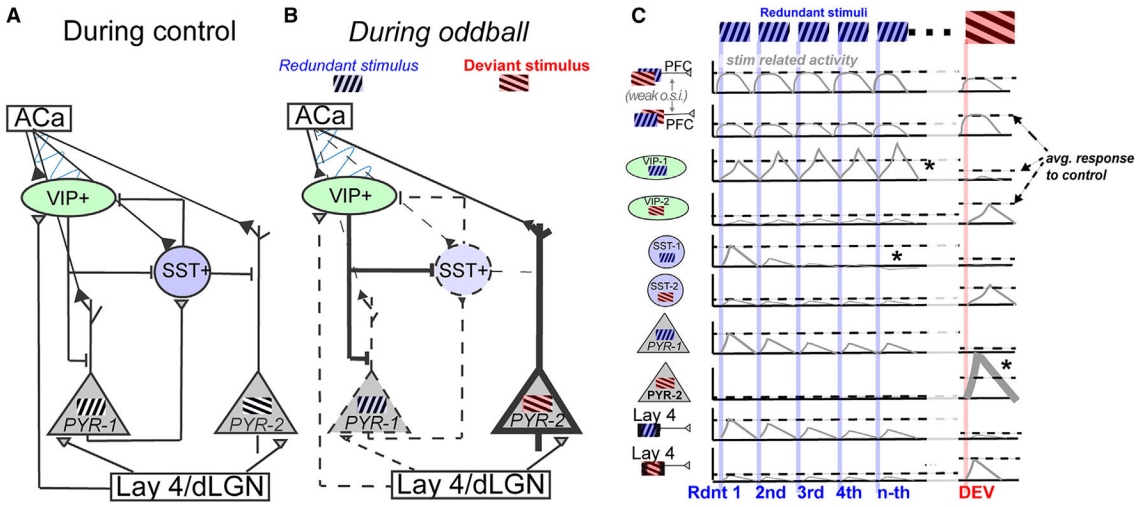

Figure 7. Proposed model of DD in V1

Shown are schematics to facilitate future work on DD circuits.

(A) Simplified V1 L2/3 circuitry. During the many-standards control, responses to any given stimulus by the circuit are at a presumed baseline, with ACa and V1 synchronous in the theta/alpha band.

(B) Line thickness depicts how a cell population's excitability is modulated during the oddball paradigm relative to the many-standards control (thicker = increase). During the oddball paradigm, inputs from the ACa drive the V1 more strongly (Figures 2G and 2H) and functionally stratify (Figures 4H and 4I) to potentiate VIPs and suppress SSTs, which, in turn, disinhibits the PYRs that are not already adapted (i.e., PYRs selective for stimuli other than the redundant). Notably, connectivity among orientation-selective VIPs, SSTs, and PYRs is a core feature of the model, which remains to be directly tested or shown.

(C) Activity dynamics during the oddball paradigm for each cell type relative to its selectivity (based on Figures 3 and 4 and past findings[4; 6]). Horizontal dotted lines depict the response of the cell population to each stimulus orientation in the control context. Asterisks indicate notable effects from data; from the top: *inverse SSA in VIPs (from Figure 3), *enhanced SSA in SST-1s to the redundant stimulus, and *DD in SST-2 and PYR-2 (from Figure 4). L4 cell activity is based on past findings.[4,6]

KEY RESOURCES TABLE

REAGENT or RESOURCE	SOURCE	IDENTIFIER
Bacterial and virus strains		
pAAV.Syn.GCaMP6s.WPRE.SV40	Addgene	100843-AAV9
pAAV.CAG.GCaMP6s.WPRE.SV40	Addgene	100844-AAV9
pAAV-CaMKIIa-hChR2(H134R)-mCherry	Addgene	26975-AAV9
pAAV-hSyn-DIO-hM4D(Gi)-mCherry	Addgene	44362-AAV8
pAAV-CamKII-ArchT-GFP (PV2527)	Addgene	99039-AAV9
Chemicals, peptides, and recombinant proteins		
Isoflurane	Patterson Veterinary/Dechra Vet	CAT#07-893-1389
Carprofen	Patterson Veterinary/Zoetis	CAT#07-844-7425
Dental Cement (C&B Metabond Quick Adhesive Cement System)	Parkell	CAT#S380
Ultrasound Gel (Aquasonic Clear)	Fisher Scientific	CAT#NC0680858
Experimental models: Organisms/strains		
SST-cre	Jackson Labs	RRID:IMSR_JAX: 013044
Vip-cre	Jackson Labs	RRID:IMSR_JAX: 010908
VGlut1-cre	Jackson Labs	RRID:IMSR_JAX:023527
GCaMP6s	Jackson Labs	RRID:IMSR_JAX:031562
C57Bl/6	Jackson Labs	RRID:IMSR_JAX:000664
Software and algorithms		
MATLAB	MathWorks	https://www.mathworks.com/products/matlab.html
PrairieView	Bruker Inc.	N/A
ImageJ	NIH	https://imagej.nih.gov/ij/index.html; RRID:SCR_003070
SPSS Statistics for Windows	IBM	https://www.ibm.com/products/spss-statistics
Original data analysis code	This study	https://zenodo.org/record/8335415 and https://doi.org/10.5281/zenodo.8335415
Original calcium imaging, LFP, and behavioral data	This study	https://doi.org/10.5281/zenodo.8273225
Other		
Glass coverslip (cranial window)	Harvard Bioscience	CAT#CS-3R
Titanium headplate	New Jersey Precision Technologies, Inc.	CAT#37907-001
Bipolar titanium electrodes (Plastics One)	Protech International Inc.	CAT#MS303/3-A/SPC
Treadmill	LabMaker	CAT#G130
Multi-field magnetic speaker - Stereo	Tucker-Davis Technologies, Inc	CAT#MF1-S
Ti: Sapphire laser (Chamleon Ultra II 680-1080nm-3.5W Coherent)	Coherent, Inc	CAT#1195408
Differential Amplifier four channel, with IC-4Mcables (Warner Instruments)	Harvard Bioscience	CAT#DP-304AIC

REAGENT or RESOURCE	SOURCE	IDENTIFIER
Noise cancellation machine (Digitimer D400 Mains Noise Eliminator/Digitimer D400 50/60Hz Noise Eliminator (Two Channel)	Digitimer North America, LLC	CAT#D400-2CH
Two-photon microscope (Bruker Ultima *In Vivo*/Ultima Investigator DL Laser Scanning Microscope)	Bruker Nano Inc	CAT#INV-02
T-Cube LED driver	Thor Labs	LEDD1B